

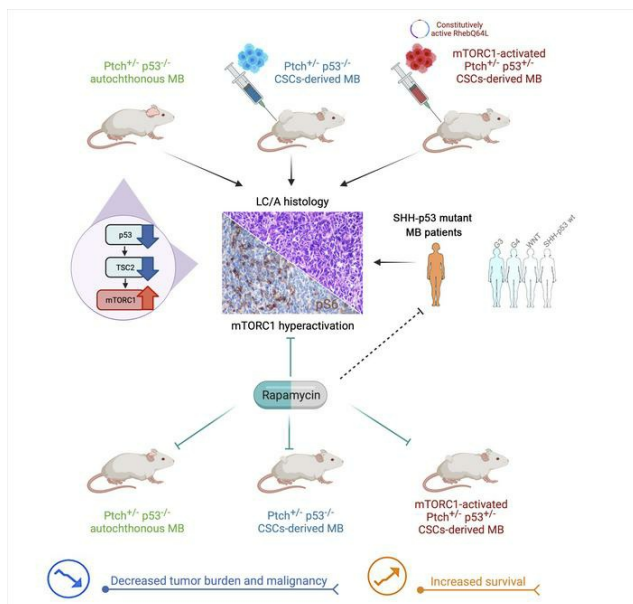
## mTORC1 promotes malignant large cell/anaplastic histology and is a targetable vulnerability in SHH-TP53 mutant medulloblastomas

Valentina Conti, ... , Pietro L. Poliani, Rossella Galli

JCI Insight. 2021. <https://doi.org/10.1172/jci.insight.153462>.

Research In-Press Preview Neuroscience Oncology

### Graphical abstract



Find the latest version:

<https://jci.me/153462/pdf>



*Submitted to JCI Insight*

**mTORC1 promotes malignant large cell/anaplastic histology and is a targetable vulnerability in SHH-TP53 mutant medulloblastoma**

Valentina Conti<sup>1</sup>, Manuela Cominelli<sup>2</sup>, Valentina Pieri<sup>1,3</sup>, Alberto L. Gallotti<sup>1</sup>, Ilaria Pagano<sup>1</sup>, Matteo Zanella<sup>1</sup>, Stefania Mazzoleni<sup>4</sup>, Flavia Pivetta<sup>5</sup>, Monica Patanè<sup>6</sup>, Giulia M. Scotti<sup>7</sup>, Ignazio S. Piras<sup>8</sup>, Bianca Pollo<sup>6</sup>, Andrea Falini<sup>3</sup>, Alessio Zippo<sup>4,9</sup>, Antonella Castellano<sup>3</sup>, Roberta Maestro<sup>5</sup>, Pietro L. Poliani<sup>2</sup> and Rossella Galli<sup>1\*</sup>

<sup>1</sup>Neural Stem Cell Biology Unit, Division of Neuroscience, San Raffaele Scientific Institute, Via Olgettina 58, Milan, Italy, 20132;

<sup>2</sup>Pathology Unit, Molecular and Translational Medicine Dept., University of Brescia, Brescia, Italy, 25124;

<sup>3</sup>Functional Neuroradiology Unit, Vita-Salute San Raffaele University and San Raffaele Scientific Institute, Milan, Italy, 20132;

<sup>4</sup>Istituto Nazionale di Genetica Molecolare (INGM), Via Francesco Sforza 35, Milan, Italy, 20122;

<sup>5</sup>Unit of Experimental Oncology 1, Centro di Riferimento Oncologico (CRO), Aviano National Cancer Institute, Via Franco Gallini 2, Aviano (PN), Italy, 33081;

<sup>6</sup>Neuropathology Unit, Fondazione IRCCS Istituto Neurologico "C. Besta", Via Celoria 11, Milan, Italy, 20133;

<sup>7</sup>Center for Omics Sciences, San Raffaele Scientific Institute, Via Olgettina 58, Milan, Italy, 20132;

<sup>8</sup>Neurogenomics Division, Translational Genomics Research Institute (TGen), Phoenix, AZ, USA;

<sup>9</sup>Laboratory of Chromatin Biology & Epigenetics, Department of Cellular, Computational and Integrative Biology (CIBIO), University of Trento, Trento, Italy, 38123.

\*To whom correspondence should be addressed:

Rossella Galli, PhD

Neural Stem Cell Biology Unit,

Division of Neuroscience,

San Raffaele Scientific Institute, Via Olgettina 58, 20132 Milan, Italy

Phone: +39 02 2643 4626

E-mail: [galli.rossella@hsr.it](mailto:galli.rossella@hsr.it)

**Abstract**

Medulloblastoma (MB), one of the most malignant brain tumors of childhood, comprises distinct molecular subgroups, with p53 mutant sonic hedgehog (SHH)-activated MB patients having a very severe outcome that is associated with unfavorable histological large cell/anaplastic (*LC/A*) features. To identify the molecular underpinnings of this phenotype, we analyzed a large cohort of MBs developing in p53-deficient *Ptch*<sup>+/-</sup> SHH mice that, unexpectedly, showed *LC/A* traits that correlated with mechanistic Target Of Rapamycin Complex 1 (mTORC1) hyperactivation. Mechanistically, mTORC1 hyperactivation was mediated by a decrease in the p53-dependent expression of mTORC1 negative regulator Tsc2. Ectopic mTORC1 activation in mouse MB cancer stem cells (CSCs) promoted the *in vivo* acquisition of *LC/A* features and increased malignancy; accordingly, mTORC1 inhibition in p53-mutant *Ptch*<sup>+/-</sup> SHH MBs and CSC-derived MBs resulted in reduced tumor burden and aggressiveness.

Most remarkably, mTORC1 hyperactivation was detected only in p53-mutant SHH MB patients' samples and treatment with rapamycin of a human preclinical model phenocopying this subgroup decreased tumor growth and malignancy.

Thus, mTORC1 may act as a specific *druggable* target for this subset of SHH MB, resulting in the implementation of a stringent risk stratification and in the potentially rapid translation of this precision medicine approach into the clinical setting.

## Introduction

Medulloblastoma (MB) is one of the most common malignant brain tumors of children, thought to originate from distinct neural stem/progenitor cell populations of the cerebellum during early embryonic development (1) (2). The peak age of diagnosis is between 6–8 years of age, although MB can also occur during the first years of life or during adulthood (1).

Genetic profiling identified different molecular consensus subgroups of MB, *i.e.* wingless and Int1 (WNT)-activated, sonic hedgehog (SHH)-activated, Group 3 and Group 4 (3), which were further subclassified into 7 to 12 molecular subtypes (4) (5). Importantly, key molecular alterations identified in MB subgroups have inferred the development of novel biomarkers that were confirmed in the fifth edition of the World Health Organization (WHO) Classification of Tumors of the Central Nervous System (WHO CNS5), which classifies MBs not only based on their histological appearance but also on their molecular features and identifies four molecular variants of the disease (WNT, SHH-*TP53* wild type, SHH-*TP53* mutant, and non-WNT/non-SHH, the latter including both Group 3 and 4 MBs) (6) (7).

Generally, WNT subgroup patients have an excellent prognosis, whereas Group 3 patients have a substantially worse prognosis (3) (8) (9). Most remarkably, SHH subgroup patients, who are associated with an intermediate prognosis, have a profoundly worse outcome when presenting with mutations in p53, due to the association with catastrophic cellular events (*i.e.* chromothripsis) and cellular anaplasia (6) (10) (11).

The current standard-of-care treatment for MB is known to lead to severe neurocognitive and neuroendocrine sequelae. Although SHH pathway inhibitors have shown promise in SHH MBs in early-phase clinical trials, treatment of infants and young children with these inhibitors needs to be approached with caution, because of the risk of skeletal defects (6). In addition, SHH inhibitors

such as Smoothed antagonists are subjected to resistance development (12) (13). Thus, the development of lowly toxic and, possibly, subgroup/subtype-tailored targeted therapeutic approaches is strongly needed.

Among the different SHH MB molecular subtypes, very high-risk patients, such as those in the SHH subset of patients with mutated *TP53*, large cell/anaplastic (*LC/A*) histology and metastatic disease (also described as SHH<sub>children</sub> or SHH $\alpha$  subtypes) (4) (5), are typically refractory to both conventional and SHH-targeted therapies and, therefore, should be prioritized for alternative upfront treatment strategies (6) (11).

Although the majority of SHH MBs with mutant *TP53* show amplification of *MYCN* and/or *GLI2* (14), there are reports of rare SHH-*TP53* mutant MBs, which are classified as *LC/A* SHH $\alpha$  and are characterized by concurrent mutations in *PTCH1* and *TP53* (11) (15). Notwithstanding these findings, several preclinical models of MB that do not bear the same exact genetic mutations found in humans are still reminiscent of many critical and relevant molecular and phenotypic features of human MBs (16) (17) (18).

With this in mind, we subjected autochthonous SHH MBs developing in *Ptch1*<sup>+/-</sup>*p53*<sup>-/-</sup> mice (19) to a comprehensive and detailed histological and molecular analysis to delineate whether features of high-risk *LC/A* SHH-*TP53* mutant MB could be detected in these mice, thus making them potential phenotypic *proxies* of this MB variant.

Notably, we identified a previously undetected large subset of *Ptch1*<sup>+/-</sup>*p53*<sup>-/-</sup> mice showing *LC/A* morphological features that we prove to significantly correlate with aberrant activation of the mechanistic Target Of Rapamycin (mTOR) signaling pathway. This correlation was found not only in preclinical models but also, and most relevantly, in human SHH-*TP53* mutant MB specimens from a collection of 90 human MB samples affiliated with all the 4 molecular subgroups.

The activation and role of mTOR pathway has been previously investigated in MB, with many studies reporting its potential targetability in vitro and in vivo by means of different mouse and human preclinical approaches (20) (21) (22) (23) (24). However, the significance of mTORC1 hyperactivation in specific molecular subtypes, such as the SHH *TP53*mut subtype of MB, has been poorly explored.

By taking advantage of subgroup-specific SHH, WNT and Group 3 mouse cancer stem cell (CSC) lines that others and we isolated by the NeuroSphere assay from different subtypes of mouse MBs (17) (18) (25) (26), we report for the first time that mTOR hyperactivation in MB is causally and specifically involved in the acquisition of *LC/A* histology and in increased malignancy in a specific subset of human SHH MBs and that addiction to this pathway in these patients may represent a cancer-specific vulnerability to be taken advantage of therapeutically.

## Results

### **Autochthonous MBs developing in $Ptch1^{+/-}$ $p53^{-/-}$ mice show large cell/anaplastic histopathological features that are associated with mTORC1 hyperactivation**

$Ptch1^{+/-}p53^{+/+}$  (abbreviated to ‘heterozygous/wildtype’, *HW*) mice develop MBs with 30-40% frequency over an average period of 5 months (Figure S1). Conversely,  $Ptch1^{+/-} p53^{-/-}$  (‘heterozygous/null’, *HN*) mice generate MBs with full penetrance and shorter time to tumor formation; in fact, they succumb to MB within 2 months after birth (Figure S1).

To date, a thorough histo-morphological classification of these different MBs has not been performed. To this end, we subjected a large collection of MB specimens, obtained from littermates of the two genotypes, to histological analysis (Table S1A,B). Hematoxylin and eosin (H&E) staining indicated that 91% of the *HW* MBs analyzed ( $n=52/57$ ) showed desmoplastic traits, such as the presence of small undifferentiated cells with hyperchromatic nuclei, maturing cells with abundant cytoplasm and dense intercellular neuropil, or classic features, such as the presence of densely packed, small “blue” round cells (Figure 1A).

Unexpectedly, all MBs developing in *HN* mice were endowed with the characteristics of *LC/A* histology, which corresponds to the most malignant histological variant of human MB (27) (Table S1). In fact, 100% ( $n=21/21$ ) of *HN* mice harbored tumors with high numbers of cells displaying marked nuclear pleomorphism (Figure 1A). Different types of large cells were observed, e.g. discohesive cells with round nuclei and prominent nucleoli (large cell subtype) or highly atypical nuclei with irregular profile (anaplastic subtype), resulting in typical features such as nuclear wrapping and nuclear molding (Figure 1A). Apoptotic cells and several mitotic figures were identified in all tumors with *LC/A* histology (Figure 1A). All these features are reminiscent of those characterizing the majority of human *SHH-TP53* mutant MBs (10).

To investigate the mechanism(s) underlying the acquisition of these histological phenotypes, we assessed the activation of a signaling pathway that regulates cell size, *i.e.* mTORC1, by testing the phosphorylated (p) form of its surrogate marker ribosomal protein S6 (pS6)<sub>S235/236</sub> in samples from all genotypes by immunohistochemistry (IHC) (Figure 1B and Table S1A,B). Tumor cells in *HW* MBs with desmoplastic/classic histology were characterized by low to absent mTORC1 activation (Figure 1B-C). Indeed, the few pS6-immunoreactive (-IR) cells found in *HW* MBs were mostly tumor-associated inflammatory cells, as shown by positive double staining with the microglia/macrophage nuclear marker IRF8 (28) (Figure 1B-C). Conversely, 90% of *LC/A HN* MBs ( $n=19/21$ ) showed many clusters of pS6-IR cells, which were negative for IRF8 expression (Figure 1B-C), indicating that mTORC1 was hyperactivated in tumor cells only in *LC/A* MBs and might play a role in the acquisition of *LC/A* features.

To confirm global mTORC1 hyperactivation in *HN* MBs, we also assessed the expression of the other known mTORC1 downstream target, p4EBP1. In line with pS6 activation, also p4EBP1 activation was significantly higher in *HN* than in *HW* MBs (Figure 1B-C and Table S1A,B).

The expression of c-Myc, which has been linked with *LC/A* phenotypes in Group 3 MBs and is also known to be activated by mTORC1, was increased in many cells in *LC/A HN* MBs, with some cells showing concomitant pS6 activation (Figure 1D-E and Figure S2A).

We also tested the activation of the mTOR complex 2 (mTORC2) pathway and found out that its downstream surrogate marker pNDRG1<sub>T346</sub> was expressed focally only in a fraction of *HN* tumors, while being undetectable in *HW* MBs (Figure S2B). Likewise, the expression of the known mTORC1-regulated protein glycoprotein nonmetastatic melanoma protein B (Gpnmb) was significantly increased in *LC/A HN* MBs as compared to *HW* MBs (Figure 1D-E).

## **The transcriptional signature of *HN* MBs is reminiscent of that of human SHH MBs with p53 mutation**

When compared with *HW* MBs showing desmoplastic/classic histology, *LC/A HN* tumors were characterized by a distinctive transcriptional signature (Figure 2A and List S1A and B). The differentially expressed genes (DEGs) between desmoplastic/classic *HW* and *LC/A HN* MBs were subjected to Gene Set Enrichment Analysis (GSEA) with distinct human transcriptional datasets including the 4 SHH, WNT, Group 3 and Group 4 subgroups as well as the 4 SHH subtypes (*i.e.* SHH $\alpha$ , SHH $\beta$ , SHH $\gamma$  and SHH $\delta$ ) (5). The gene set qualifying the SHH subgroup of patients *vs.* the other 3 subgroups (WNT, Group 3 and Group 4) was upregulated in *LC/A HN* tumors (Figure 2B and Table S2). Likewise, genes upregulated in the SHH $\alpha$  subtype, and, within this subtype, those upregulated in SHH $\alpha$  tumors with p53 mutation and *LC/A* pathology *vs.* SHH $\alpha$  tumors with wildtype p53 and desmoplastic/classic histology (5) were again enriched in *LC/A HN* tumors (Figure 2C, Table S3 and S4, List S2 and S3). As an example, *Dach2* and *Otx1*, which were 2 of the 4 genes found in the core enrichment list after performing GSEA on the SHH $\alpha$  gene signature derived from the differential gene expression between the SHH $\alpha$  subtype of patients and the remaining 3 SHH subtypes (List S2) (5), were significantly upregulated in the SHH $\alpha$  subgroup in the *in silico* analysis of 223 human SHH MB samples by the R2 platform (<http://hgserver1.amc.nl/cgi-bin/r2/main.cgi>) and were also among the top-ranking genes upregulated in *HN* tumors, as validated by qPCR analysis (Figure 2D).

Interestingly, the protein abundance of Yap1, N-Myc and Gli2, which are associated with SHH-*TP53* mutant and SHH $\alpha$  MBs (5), was significantly increased in *LC/A HN* MBs (Figure 2E-F), with Yap1 also found in cells hyperactivating pS6 (Figure 2E-F and Figure S2C).

Thus, *LC/A HN* MBs reproduce phenotypically many molecular features qualifying human *LC/A* SHH-*TP53* mutant MBs.

### **The expression of the negative mTORC1 regulator Tsc2 is significantly decreased in *HN* MBs and is regulated by p53**

To dissect the mechanism(s) responsible for mTORC1 hyperactivation in *LC/A HN* MBs, we compared desmoplastic/classic *HW* and *LC/A HN* MBs for the expression of *i*) the mTORC1 negative upstream regulators Tsc1, Tsc2, Tbc1d7 that are components of the Tuberous Sclerosis Complex, and *ii*) the negative mTORC1 mediators pRaptors<sup>792</sup>, Grb10 and Pten. Whereas no significant differences were observed in the expression of Tsc1, Tbc1d7 (Figure 3A), pRaptor, Grb10, and Pten (data not shown), the protein expression of Tsc2 was significantly reduced in *LC/A HN* MBs as compared to *HW* MBs (Figure 3A). Accordingly, *in silico* analysis of human SHH MB samples showed significantly reduced *TSC2* expression in SHH $\alpha$  specimens (Figure 3B).

To define the molecular underpinnings for Tsc2 downregulation in *HN* MBs, we focused our attention on p53. In fact, *Tsc2* expression in cell lines and normal tissues can be directly regulated transcriptionally by p53 (29). To test if this holds true also in MB, we took advantage of p53-proficient non-tumorigenic *HW* CSCs that we previously isolated from *HW* MBs by the Neurosphere Assay (26). Mouse *HW* CSCs were transduced either with a retroviral vector coding for the green fluorescent protein (*GFP*) or for a dominant negative form of p53 (DNp53) (17). The observed increased endogenous levels of p53, which, nonetheless, is functionally inactive, are due to wildtype protein stabilization induced by the binding with DNp53 (30). Tsc2 expression was significantly downregulated upon p53 inactivation, and this was paralleled by a significant increase in pS6 activation (Figure 3C), suggesting that p53 mutations in MBs might promote mTORC1 activation through negative regulation of Tsc2 levels. Most relevantly, p53 inactivation conferred tumorigenic ability to DNp53 *HW* CSCs, which gave rise to tumors showing anaplastic features and concomitant pS6 hyperactivation (6 out of 10 transplanted mice with 60% penetrance) (Figure 3D).

In support of the role of p53 in activating mTORC1 through Tsc2 regulation, while analyzing our cohort of *HW* MBs, we detected a small subset of tumors ( $n=5/57$ ) that was characterized by *LC/A* histology (Figure 3E), in place of the desmoplastic/classic histology expected in this type of MBs (Figure 1A). Interestingly, *LC/A* areas were characterized by the presence of many pS6-IR cells (Figure 3E). In full agreement with a previous report (31), all these ‘outliers’ were endowed with the presence of more than 80% of tumor cells displaying intense nuclear staining for p53, suggestive of spontaneously occurring inactivating mutations in p53, with most pS6-IR cells being also p53-IR (Figure 3E-F). By performing genomic DNA next generation sequencing (NGS) of the full coding frame of p53 on 3 of these outliers, we confirmed the presence of pathogenic heterozygous somatic p53 mutations, such as C132F, Y233C and C173G (Figure S3). To be noted, Tsc2 expression in these p53 mutant *HW* MBs was significantly lower than in normal *HW* MBs (Figure 3G), in line with the observations in *HN* MBs (Figure 3A).

Confirming these findings, a CSC line (L68) that we established from one of the *HW* ‘outliers’ with p53 mutation acquired tumorigenic potential in vivo (32) (9 out of 12 transplanted mice with 75% penetrance), as opposed to normal *HW* CSC lines that are devoid of this ability Ward, et al. (25) (32). Tumors generated from this CSC line showed anaplastic traits and were characterized by the presence of many tumor cells that were IR for pS6 and, in most cases, co-labelled with p53 (Figure 3H). The expression of Tsc2 was again significantly decreased in tumors derived from L68 CSC line (Figure 3I), thus further corroborating p53 role in the regulation of mTORC1 activation *via* Tsc2.

### ***HN* MB-derived CSCs give rise to *LC/A* MBs that hyperactivate mTORC1**

To assess the endogenous mTORC1 activation in mouse CSCs isolated from *HN* MBs and in the tumors derived from them, we transplanted different GFP-transduced CSC lines subcutaneously

(26) (33) into immunocompromised mice. Since *HW* CSCs are not tumorigenic (25) (26), as reference CSC lines for *HN* CSCs we used CSCs isolated from *Ptch1<sup>+/-</sup>p53<sup>+/-</sup>* ('heterozygous/heterozygous', *HH*) mice that are endowed with tumorigenic potential (26). In addition to *HH* and *HN* CSC lines, we also established Myc CSC lines from Group 3 Myc-driven intracranial MBs that we generated by injecting p53-null postnatal day 7 cerebellar neural stem cells (NSCs) (26) transduced with a retroviral vector coding for the constitutively active form of Myc, *Myc<sup>T58A</sup>* (17).

*HH* CSC lines (LB, L21, L84 and L1) did activate mTORC1 at low level, while expressing variable levels of Myc (Figure 4A). Similarly, *Myc<sup>T58A</sup>* CSC lines (ML) as ML1 and ML4 had constitutively high Myc expression but did not hyperactivate pS6. On the contrary, *HN* CSC lines as L83 and L66 showed a remarkably high activation of pS6, with low levels of Myc (Figure 4A).

In line with in vitro findings, tumors derived from the implantation of *HH* CSCs (LB and L21) showed "classic" morphology (26), low Myc expression and mTORC1 activation that was solely observed in IRF8-positive macrophages/microglia cells (Figure 4B-C). Tumors derived from a small subset of *HH* CSC lines (L84) were characterized by *LC/A* features and high Myc protein level; however, mTORC1 activation was never detected in tumor cells, while being again confined to the stromal compartment. Likewise, MBs originating from Myc CSC lines were *LC/A* with constitutive Myc activation, but again showed mTORC1 activation only in stromal cells (Figure 4B, C and E, Table S5). Most notably, MBs induced by *HN* CSC lines (*i.e.* L66 and L83) displayed *LC/A* features associated with significantly high mTORC1 activation specifically in tumor cells (Figure 4B, D and E, Table S5), thereby recapitulating autochthonous *HN* tumors.

Thus, also in experimental tumors induced from the implantation of mouse CSCs, *LC/A* morphology correlated with increased mTORC1 activation.

**Enforced hyperactivation of mTORC1 in *HH/HN* CSCs increases tumor malignancy, induces an *LC/A* phenotype, and modulates the expression of subgroup-restricted markers**

To prove that mTORC1 hyperactivation was causally linked to the acquisition of *LC/A* features, we transduced both *classic HH* CSCs (LB and L21) and, as a control, *LC/A HN* CSCs (L83) with a lentiviral vector coding for the constitutively active form of the mTORC1 activator Rheb, *Rheb<sup>Q64L</sup>* (34) or with a mock vector coding for GFP. Both *classic* and *LC/A Rheb<sup>Q64L</sup>*-transduced CSCs showed significant hyperactivation of pS6, when compared with controls (Figure 5A, Figure S4A and S5). Interestingly, all *Rheb<sup>Q64L</sup>* CSC lines showed increased expression and phosphorylation of NDRG1, the latter suggestive of concomitant mTORC2 hyperactivation (Figure 5A, Figure S4A and S5).

*Rheb<sup>Q64L</sup> HH* CSC-derived tumors developed in a shorter time frame and grew larger than controls (Figure 5B and Figure S4B), whereas no difference in growth was observed in *Rheb<sup>Q64L</sup> LC/A HN* CSC-derived tumors with respect to mock (Figure 5B).

Most significantly, as opposed to the ‘*classic*’ morphological features observed in GFP-transduced *HH* CSC-derived tumors (26), *Rheb<sup>Q64L</sup> HH* CSC-derived tumors, which comprised many cells hyperactivating both pS6 and p4EBP1, acquired *de novo* typical features of *LC/A* tumors, such as the presence of large cells, nuclear molding, anaplastic traits, high mitotic activity, and increased apoptosis (Figure 5C and Figure S4C, Table S1). Indeed, almost all pS6-IR cells found in *Rheb<sup>Q64L</sup> HH* CSC-derived tumors were large and showed typical morphological *LC/A* features, such as the presence of angular nuclei and prominent nucleoli (Figure 5C and Figure S4C). Like *LC/A* autochthonous *HN* MBs, *Rheb<sup>Q64L</sup> HH* CSC-derived tumors did show increased activation of mTORC2, as well as enhanced expression of *Gpnmb* (Figure 5C and Figure S4C).

After transduction with *Rheb<sup>Q64L</sup>*, spontaneously *LC/A HN* CSCs (L83) gave rise to tumors that acquired additional *LC/A* features, such as the presence of large cells with multiple nucleoli,

characterized by nuclear molding (Table S1), as well as increased pS6, p4EBP1, pNDRG1 and Gpnmb expression (Figure S5A).

Concerning tumor subgroup affiliation, hyperactivation of mTORC1 via *Rheb*<sup>Q64L</sup> in *classic HH* CSCs resulted in the significant downregulation of WNT pathway-specific markers such as  $\beta$ -catenin (Figure 5D and Figure S4C) with concurrent upregulation of p53 mutant SHH subgroup-specific markers, such as Yap1, N-Myc, Gli2 and Sox2 (Figure 5D and Figure S4C). Also, expression of c-Myc was enhanced in *Rheb*<sup>Q64L</sup> *HH* CSC-derived tumors, as observed in autochthonous *HN* MBs (Figure 5D and Figure S4C). Similar findings were observed in *LC/A HN* CSCs after transduction with *Rheb*<sup>Q64L</sup>, which showed significantly enhanced mTORC2 hyperactivation and increased Gpnmb expression (Figure S5A). Although most of subgroup markers were already upregulated in mock *HN*, a significant difference was noticeable for Gli2, Sox2 and c-Myc (Figure S5B).

When the same *classic* mock and *Rheb*<sup>Q64L</sup> *HH* CSCs (LB) were injected intracranially (Figure S6), mTORC1-hyperactivating tumors again showed highly malignant histological features and developed in a very short time window (53±14 days for *Rheb*<sup>Q64L</sup> tumors vs. 197±18 days for *GFP* tumors). As opposed to mock tumors showing *classic* histological features, *Rheb*<sup>Q64L</sup>-transduced tumors acquired typical *LC/A* traits, with diffuse anaplastic areas and regions containing cells with nuclear molding (Figure S6).

As such, mTORC1 hyperactivation directly promotes the acquisition of highly malignant *LC/A* characteristics in MB.

### **Pharmacological targeting of the mTOR pathway hampers the growth of autochthonous SHH-TP53 mutant MBs**

To test whether increased mTORC1 activation in *LC/A* MBs could give rise to a potentially targetable vulnerability in SHH-*TP53* mutant human MBs, we designed a preclinical Phase 2-like trial in which different types of autochthonous mouse MBs were treated with the brain-permeant mTOR inhibitor rapamycin (6 mg/kg) for 5 days a week for up to 80 days of treatment (Figure 6 and Figure S7 and S8).

To mimic both lowly and highly severe clinical settings, *i.e.* the presence of either minimal residual disease/small tumors or large unresectable tumors, we set up a randomized three-arms interventional trial by treating *LC/A HN* mice at early and late stages of tumor development and by longitudinally monitoring tumor growth by 7 Tesla conventional T2-weighted MRI. Early-treated *HN* mice started rapamycin between 10 and 12 days of age, whereas late-treated *HN* mice began treatment at 23-27 days of age. As a negative control, we treated *classic HW* mice, which activate mTORC1 only in stromal cells and, thus, should not respond to treatment.

In fact, *HW* mice treated with rapamycin showed only a slight reduction in tumor volume (Figure S7A-B). Conversely, a statistically significant decrease in tumorigenesis was detected in rapamycin-treated *HN* mice bearing either small or large tumors, as compared to vehicle-treated controls, with a significantly higher reduction in volume in early-treated than in late-treated *HN* mice (Figure 6A-B and S7C-D). Tumor response to treatment was associated with 34% and 23% increase in median survival of early- and late-treated *HN* mice, respectively (Figure 6C).

IHC analysis demonstrated that activation of the mTORC1 downstream surrogate marker pS6 was downregulated in *HN* tumors following rapamycin delivery *in vivo*, suggesting effective target engagement during treatment (Figure 6D and Figure S8A and C). On the contrary, phosphorylation of 4EBP1 on Thr37/46, which is known to be rapamycin-insensitive, was unaffected by the treatment (Figure 6D and Figure S8A). mTOR inhibition induced changes in *HN* MB morphology, with a significant decrease in nuclear molding and pleomorphism as well as an overall reduction

in anaplastic traits (Figure 6D). Expression of Yap1, N-Myc and Gli2 was also reduced by treatment (Figure 6D and Figure S8B).

### **Pharmacological targeting of the mTOR pathway significantly impairs the growth of CSC-derived mTOR-driven *LC/A* MBs but not that of MBs belonging to other subgroups**

To capture the inter-tumor molecular heterogeneity of a MB patient population, we designed a master interventional preclinical trial by treating with rapamycin several molecularly different mouse CSC-derived MBs. These tumors were *proxies* of *a)* spontaneously mTORC1-activating '*LC/A*' SHH-*TP53* mutant MBs; *b)* enforced mTORC1-activating *Rheb*<sup>Q64L</sup>-transduced '*LC/A*' SHH-*TP53* mutant MBs; *c)* enforced mTORC1 activating *Rheb*<sup>Q64L</sup>-transduced '*classic*' SHH-*TP53* mutant MBs; *d)* '*classic*' WNT-like MBs (26); *e)* Myc-driven '*LC/A*' MBs and *f)* *Myc*<sup>T58A</sup>-transduced '*LC/A*' CSC MBs. We transplanted all the different types of CSCs into the flank of immunocompromised mice and allowed tumors to become palpable before performing randomization and starting rapamycin treatment.

In line with findings obtained in autochthonous *HN* MBs, rapamycin administration resulted in the significant reduction in growth of spontaneously '*LC/A*' and enforced '*LC/A*' *Rheb*<sup>Q64L</sup> *HN* and *HH* CSC-derived tumors, but not of '*classic*' WNT, Myc-driven '*LC/A*' and Group 3 Myc MBs (Figure 7A).

mTOR inhibition promoted a significant reduction in nuclear pleomorphism and cell size as well as decreased nuclear molding in the presence of an enlarged intercellular matrix (Figure 7B). As expected, protracted rapamycin treatment impaired not only mTORC1 but also mTORC2 activation (Figure 7B and Figure S9). mTORC1 inhibition also induced downregulation of *Gpnmb* (Figure 7B and Figure S9). Expression of Yap1 and Sox2 was slightly reduced, whereas no significant difference in expression was observed for c-Myc (Figure 7B and Figure S9).

Collectively, these data indicate that inhibition of mTORC1 signaling may lead to a significant improvement in disease control in SHH-*TP53* mutant MBs as compared to the other MB subgroups.

**mTORC1 activation is specifically found in human p53 mutant SHH MBs with *LC/A* component and may be a subgroup-specific therapeutic vulnerability**

To determine whether mTORC1 hyperactivation could be detected in human *LC/A* SHH-*TP53* mutant MBs, thus potentially serving as diagnostic marker for this specific cohort of patients, we performed IHC for pS6 on 90 human MB specimens, comprising all the distinct molecular subgroups of MB. SHH-*TP53* mutant MBs represent 21% of SHH MBs that account for 29% of all MBs (10). Considering that only 40% of SHH-*TP53* mutant MBs show *LC/A* histology, the frequency of patients with *LC/A* SHH-*TP53* mutant MBs is very low (3% of all MBs) (10). As such, we were able to collect 8 specimens of *LC/A* SHH-*TP53* mutant MBs from 2 different Institutions. As controls, we analyzed 15 desmoplastic/classic SHH-*TP53* wildtype MBs, 4 classic WNT MBs, 51 classic/desmoplastic non-WNT/non-SHH MBs, and 12 *LC/A* non-WNT/non-SHH MBs (Table S6).

The same correlation between the presence of *LC/A* features and mTORC1 hyperactivation observed in mouse preclinical models was detected only in human MB specimens classified as SHH with p53 mutation, which all showed high frequency of pS6- and p4EBP1-IR tumor cells (Figure 8A-B). Conversely, samples from all the other subgroups never hyperactivated pS6 in tumor cells but only rarely in stromal cells (Figure 8A-B and Table S6). N-MYC, GLI2 and YAP1 proteins were detected also in other molecular subgroups (Figure S10A-B); if considering only SHH MBs, all three proteins were significantly upregulated in SHH-*TP53* mutant MBs as

compared with SHH-*TP53* wild type MBs (Figure S10C). Thus, mTORC1 activation is associated with *LC/A* histology only in human SHH-*TP53* mutant MBs.

To further confirm this finding, we subjected the genes differentially expressed between human SHH $\alpha$  MBs with *LC/A* histology vs human SHH $\alpha$  MBs with desmoplastic/classic histology to GSEA (5) with human transcriptional datasets containing mTOR-related signatures (Figure 8C) and observed a statistically significant enrichment for mTOR- and mTORC1-specific genes was found in human SHH $\alpha$  MBs that were characterized by *LC/A* histology and, for 75% of them, also by p53 mutation (Table S7).

To explore the functional relevance of mTORC1 activation in human SHH-*TP53* mutant MBs, we took advantage of the human primary MB cell line DAOY. Although being classified as a SHH MB cell line with p53 mutation (35), the DAOY cell line was originally established from a desmoplastic MB (36). Since desmoplastic SHH MBs very rarely show p53 mutations (14), it is likely that DAOY cells acquired p53 mutations after culturing in vitro. Accordingly, in vivo implantation of naïve DAOY cells gave rise to MBs that did not show mTORC1 activation in tumor cells and were endowed with desmoplastic/classic histology, implying that p53 mutations should be present in the original tumor to be able to influence the molecular make-up of the tumor (Figure 8D and Table S1). DAOY cells were transduced with the *Rheb*<sup>Q64L</sup> lentiviral vector and, as observed in mouse MB CSCs, mTORC1 hyperactivation increased the expression of NDRG1 and its phosphorylation (Figure S11A). *Rheb*<sup>Q64L</sup> DAOY cells gave rise to tumors that grew faster and were more malignant than controls (Figure S11B), showed acquisition of some *LC/A* features, such as the presence of large cells with multiple nucleoli as well as increased mitotic figures and apoptotic cells, hyperactivated mTORC2 (Figure 8D and Table S1) and displayed increased expression of GPNMB, YAP1, N-MYC, GLI2, SOX2, and c-MYC (Figure 8D-E). Thus, enforced mTORC1 activation in DAOY cells may give rise to a reliable human preclinical model of *LC/A*

SHH-*TP53* mutant MBs, which is also characterized by increased expression of N-MYC and GLI2, as expected in N-MYC/GLI2 amplified SHH-*TP53* mutant MBs.

Finally, we took advantage of this human MB model to test whether mTORC1 inhibition could reduce the growth of human *LC/A* SHH p53 mutant tumors in vivo. A 3-fold reduction in tumor volume was observed in *LC/A Rheb<sup>Q64L</sup>* DAOY-derived MBs treated with rapamycin as compared to vehicle-treated controls, while no difference was observed between vehicle- and rapamycin-treated ‘*classic*’ *GFP* DAOY-derived MBs (Figure S11C). Rapamycin treatment inhibited mTOR activation, as shown by a significant decrease in both pS6 and pNDRG1 and by only a mild reduction in p4EBP1 (Figure 8D). A significant decrease in large cells and anaplastic traits, such as nuclear pleomorphism and mitotic figures (Figure 8D), and in the levels of GPNMB, YAP1, N-MYC, GLI2, SOX2 and c-MYC was observed after mTORC1 inhibition (Figure 8D-E).

## Discussion

In recent years, no efforts were spared to improve the identification of the molecular players underlying MB development and evolution. Different molecular subgroups and subtypes of the disease have been identified that are endowed with specific genomic, epigenomic, transcriptomic and proteomic profiles (37). This wealth of knowledge is currently used to inform the development of novel therapeutic avenues that take into consideration the molecular status of MB, aiming at implementing molecularly targeted clinical protocols relying on patient stratification and selection (37).

In line with this view, most preclinical studies are now focusing on the definition of the molecular make up of MB, to identify meaningful molecularly targeted approaches to be translated into the clinical settings. Within this frame of mind, we reasoned that already available mouse models of MB might be instrumental to this aim, if characterized in greater detail both from a morphological and molecular perspective.

In this study, we provided a comprehensive investigation of one on the most widely used mouse model of SHH MBs, *i.e.* the *Ptch*<sup>+/-</sup> mouse model with or without concurrent mutation in *TP53* (19), by subjecting to histo-morphological analysis large cohorts of mice with different genotypes. By this approach, for the first time we report that *Ptch*<sup>+/-</sup> *p53*<sup>-/-</sup> ('heterozygous/null', *HN*) mice show distinctive features of large cell/anaplastic (*LC/A*) MBs, which are not observed in *Ptch*<sup>+/-</sup> *p53*<sup>+/+</sup> ('heterozygous/wildtype', *HW*).

Although concurrent loss of *PTCH1* and *TP53* has been found in a few *LC/A* SHH $\alpha$  human MBs (15), our model might not completely reproduce the genetics of the disease, which in most cases is known to be associated with amplification in *MYCN* and *GLI2* (14) (37) (38). While it is desirable that a preclinical model mimics all the features of the corresponding human tumor in

terms of genetics, cell of origin, clinical manifestations, histological phenotype and response to therapy, none of the currently available models of MB fulfill all these requirements at the same time (39). Indeed, many studies are available in which specific mutations that are not normally observed in human patients have been exploited to implement subgroup-specific models. For instance, mouse models of Myc and Wnt subgroups can be generated only after introducing p53 mutations that are very rarely detected in the corresponding tumors in patients (16) (17) (18). Nevertheless, these preclinical models are valuable phenocopies of the human disease, thus indicating that modeling of a disease-specific phenotype may take place also in the absence of a disease-specific genotype. In our study, by combining different experimental mouse models, as autochthonous and CSC-derived MBs, with human MB samples (human post-surgery specimens and human cell lines), we have generated a comprehensive histological, molecular and functional experimental platform that provided sound evidence that mTOR activation is a therapeutic target in *LC/A SHH-TP53* MBs, independent from the genetic mutations responsible for SHH pathway hyperactivation, e.g. upstream mutations in *PTCH1* or downstream amplification of *N-MYC* and *GLI2*. Indeed, *Ptch1<sup>+/-</sup> p53<sup>-/-</sup>* MBs are characterized by upregulation of N-Myc and Gli2, as to mimic what it is supposed to take place in *N-MYC* and/or *GLI2* amplified SHH MBs.

To pinpoint the molecular mechanisms underlying the malignant morphological features observed in *HN* MBs, we focused on the mTOR pathway, which is known to control cell size and growth. mTOR signalling is hyperactive in a large proportion of human cancers and, accordingly, mutations in distinct components of the pathway have been etiologically involved in several cancers (40).

In this study, we provide first evidence that the activation of mTOR is specifically associated with a subset of human SHH MBs that are frequent in children and are characterized by *LC/A* histology and p53 mutation. The significance of mTOR hyperactivation in MB is controversial, as reviewed

in (20) (22). Concerning the assessment of mTOR activation in specific preclinical mouse models of MB, activation of mTORC1 and its interaction with the SHH pathway were assessed in a *SmoM2* mouse model during normal cerebellar development and were positively associated with MB initiation (21). However, this seminal study, which paved the way to ours, while finely dissecting the interplay between mTORC1 and SHH pathways, focused entirely on p4EBP1, which is considered one of the two surrogate markers for mTORC1 activation but, notably, is also regulated by other kinases in a mTOR-independent way (41). In fact, the data on p4EBP1 activation in the different molecular subgroups of human MBs reported in the Wu's study are at odds with ours, which were obtained by using not only p4EBP1 but also the other mTORC1 surrogate marker pS6, *i.e.* the gold standard in the field, and by also including the histological affiliation of the human MB samples analyzed.

Targeting mTOR has also been suggested, in a review, as a potential therapeutic strategy for Group 4 MBs (22) and, accordingly, mTORC1 hyperactivation has been recently reported in human cell lines genetically modified to model Group 4 MBs (42). Although some studies reported the efficacy of mTOR inhibitors in different human MB cell lines *in vitro* (23), no detailed analysis with respect to the molecular subgroup and the persistence of mTOR activation was undertaken *in vivo*. Indeed, in our study we report that the activation of mTOR in CSCs and human MB cell lines *in vitro* does not predict its activation in the corresponding tumor after transplantation.

As for the significance of mTOR activation specifically in human SHH MBs, mTORC1 has been variably associated with different molecular subtypes of the SHH subgroup, such as infant (24) and adult SHH MBs (14). As opposed to our findings, in the first study, mTOR activation, which was dependent on OCT4 expression in *MYCN*-overexpressing iPS cells, led to the formation of xenografts with clear desmoplastic traits (24). However, although mTORC1 activation by IHC for p4EBP1 was reported in iPS-derived xenografts and in patient-derived xenografts, it was not

analyzed in human post-surgery samples of infant SHH MB. As a matter of fact, in our collection of infant SHH MBs ( $n=13$ ), all showing desmoplastic histology, we never detected mTORC1 activation in tumor cells. Thus, mTOR activation in iPS-derived humanized preclinical models might be secondary to the genetic modifications induced in iPS cells rather than being a molecular trait associated with the infant subgroup of the human disease. In the second study, mTOR activation was observed in 30% of adult MBs, which are neither characterized by *LC/A* histology nor by p53 mutations. However, in the same study some cases of children MBs were also reported to be positive for pS6. It may be possible that the pS6-positive children SHH MBs belonged to the “*LC/A*-p53 mutant” cohort of patients, thus increasing their relative frequency and being, therefore, in agreement with our findings.

As for the mechanisms responsible for mTOR hyperactivation, we have identified a consistently reduced expression of the mTORC1 inhibitor Tsc2 in *Ptch1<sup>+/-</sup> p53<sup>-/-</sup>* MBs that has been detected at the mRNA level also in SHH $\alpha$  MB patients. Indeed, genetic inactivation of Tsc2 protein, which results in the destabilization of the TSC complex and in the ensuing Rheb-dependent activation of mTORC1, has been shown to affect in cerebellar granule cell expansion and MB initiation (43). As for the low level of Tsc2 observed in our p53-mutant mouse models, the expression of Tsc2 might be directly regulated transcriptionally by p53 binding to its promoter (29) (44). Indeed, here we demonstrated that loss of p53 activity in p53-proficient *HW* MB CSCs and in a subset of *HW* MB ‘outliers’ with spontaneous p53 mutations enhances mTORC1 activity by decreasing Tsc2 expression, thus providing first evidence that the p53-dependent regulation of Tsc2 may be active also in MB.

mTOR inhibitors are currently under clinical testing for many cancer types, including pediatric brain tumors. Few basket trials are ongoing or have been recently completed that included very small numbers of MB patients, with only one trial that recruited patients based on the presence of

inactivating mutations in the PI3K/mTOR pathway, although with no reference to the original molecular subgroup/subtype. Given the low number of MB patients and the lack of comprehensive molecular and histological information, the results of these studies might be discouraging. On the contrary, clinical studies, potentially targeting a specific and molecularly uniform subpopulation of MB patients as the one we identified here, might generate valuable information that may directly impact treatment decisions and disease prognosis (45).

As mentioned before, although a targeted approach aiming at inhibiting mTOR activation might be life-changing for SHH-*TP53* mutant MB patients, they are quite infrequent. To increase the applicability of this therapeutic paradigm, we may take into consideration the fact that patients with recurrent MB often present with *LC/A* histology and with *TP53* mutations that were undetected in the primary tumor (46). In fact, loss of function of *Trp53* is identified as a key event in the pathogenesis of recurrence (38) (46) (47) (48). Specifically, genetic events in *TP53* pathway genes or in the actual *TP53* gene are frequent in recurrences, predominantly in SHH MBs (38) (48). Very interestingly, the mouse model used for modeling post-treatment MB recurrence, namely a *Trp53*mut transposon-driven MB model, shows large cells, nuclear atypia and nuclear molding that are all typical features of *LC/A* histology (49). Accordingly, another report demonstrated that combined p53 and MYC defects emerge at MB recurrence and that relapsed SHH MBs with altered p53/MYC were significantly associated with *LC/A* pathology (47). Likewise, metastasis through leptomeningeal dissemination has been associated with *LC/A* SHH MBs (5) (49). Thus, testing the hyperactivation of mTOR in recurrent/metastatic MBs might increase the numbers of patients that may benefit from this personalized medicine approach.

The current indications for unlocking precision medicine-based approaches in the clinical practice propose that disentangling the plethora of signalling mechanisms regulating the different variant of a tumor might require a more comprehensive understanding of smaller subsets of

patients, segregated by specific molecular processes, and a deeper understanding of how these distinct cohorts relate to each other (50). This concept has been recently emphasized in the WHO CNS5, which discusses that, although it may be challenging to identify biologically defined groups that may be too small for clinical trials to be designed, it is important to build upon the availability of subgroup/subtype specific molecular vulnerabilities, whose clinical impact may be lost if molecularly distinct patients are treated the same way (7).

We believe that the findings here reported are in full agreement with this view, by relying *a)* on strong evidence collected in several preclinical mouse models mimicking the different MB subgroups, *b)* on the functional validation of the molecular mechanisms involved by using the same models, *c)* on the pharmacological treatment by different experimental paradigms, *d)* on the validation in human preclinical models and, most remarkably, *e)* on the stringent assessment of the association of the molecular alterations with specific patient cohorts.

## Methods

### Mouse strains

The experimental breeders used in this study were B6.129-*Ptch1<sup>tm1Mps</sup>* (JAX stock #003081) and B6.129S2-*Trp53<sup>tm1tyj</sup>* (JAX stock #002101) mice (The Jackson Laboratory). All mice were maintained on a C57/BL6 background for at least five generations prior to initiate experiments. *Ptch1<sup>+/-</sup> p53<sup>+/+</sup>* (abbreviated to ‘heterozygous/wildtype’, *HW*), *Ptch1<sup>+/-</sup> p53<sup>+/-</sup>* (‘heterozygous/heterozygous’, *HH*), and *Ptch1<sup>+/-</sup> p53<sup>-/-</sup>* (‘heterozygous/null’, *HN*) mouse littermates were generated by crossing *HH* mice with ‘wildtype/ heterozygous’ (*WH*) or with ‘wildtype/null’ (*WN*) mice.

CD1-*Foxn1<sup>nu</sup>* and NOD.Cg-Prkdc<sup>SCID</sup> (NSG) immunocompromised mice were purchased from Charles River Italy and Charles River France, respectively.

### Immunostaining on paraffin-embedded sections

From formalin-fixed paraffin-embedded mouse and human tumor samples (University of Brescia), 2  $\mu$ m sections were cut, de-waxed, re-hydrated and endogenous peroxidase activity blocked by 0.3% H<sub>2</sub>O<sub>2</sub>/methanol for 20 minutes. Heat-induced antigen retrieval was performed using a microwave oven or a thermostatic bath in 1.0 mM EDTA (pH 8.0), 1.0 mM Citrate (pH 6.0) or 1mM Tris-EDTA (pH 9.0) buffer (see Supplementary Methods). Sections were then washed in TBS (pH 7.4) and incubated for 1 hour or over-night in TBS/1% BSA with the specific primary antibody (see Supplementary Methods). Single immunostaining was revealed by Envision<sup>+</sup>System-HRP Labelled Polymer Anti-Rabbit or Anti-Mouse (DAKO) or the NovoLink<sup>TM</sup> Polymer Detection System (Novocastra<sup>TM</sup> Laboratories Ltd) followed by diaminobenzidine (DAB) as chromogen and hematoxylin as counterstaining. For double immunostainings, after completing the

first immune reaction, the second primary antibody was applied and labelled using MACH 4™ Universal AP Polymer Kit (Biocare Medical); chromogen reaction was developed with Ferangi Blue™ Chromogen System (Biocare Medical) and nuclei were counterstained with hematoxylin. From Carnoy-fixed human tumor samples (Istituto Neurologico Besta), 2-µm-thick sections were cut, deparaffinized, rehydrated, treated for antigen retrieval (pH 9 buffer at 98°C for 20 min), incubated with normal goat serum (Agilent, USA) and then with the primary antibody. Sections were subsequently incubated with Envision® FLEX HRP-conjugated secondary antibody (Agilent, USA), then reacted with diaminobenzidine (DAB Substrate Chromogen System, Agilent, USA) and counterstained with haematoxylin.

### **Image data acquisition and analysis**

All histological and IHC staining results were reviewed independently by two pathologists that were blinded to the identity of the mouse samples and to the clinicopathological information of human samples. Images were acquired at 40x magnification for standard IHC and at 60x magnification for double IHC staining by a Nikon camera mounted on Nikon microscope using the NIS-Elements software. Image analysis was performed by using the open-source image processing package ImageJ-Fiji ([www.fiji.sc](http://www.fiji.sc)).

### **Western blotting**

Each frozen tissue/cell pellet was homogenized in 10x volume of RIPA lysis buffer (10 mM Tris-Cl pH 7.2, 150 mM NaCl, 1 mM EDTA pH 8) with 1% Triton X-10/0.1% deoxycholate, 0.1% SDS, and protease and phosphatase inhibitor mixture (Roche). Samples were then diluted in Laemmli's SDS sample buffer. Proteins were separated by electrophoresis on 10% polyacrylamide gels according to the TGX Stain-Free FastCast Acrylamide kit protocol (Bio-Rad), and transferred

onto Trans-Blot nitrocellulose membranes (Bio-Rad) according to the Trans-Blot Turbo Transfer System kit protocol (Bio-Rad). Primary antibodies were diluted in 3% BSA (Sigma-Aldrich) or 5% nonfat dry milk in TBS-T, and the membranes were incubated overnight at 4°C (see Supplementary Methods). The primary antibody was removed, and the blots were washed in TBS-T and then incubated for 1 hour in HRP-conjugated secondary antibodies (Amersham). Reactive proteins were visualized using a Clarity Western ECL substrate kit (Bio-Rad), and exposure was performed using UVItec (Cambridge MINI HD). Images were acquired by NineAlliance software.

### **RNA sequencing**

Total RNA from mouse MBs was extracted using the RNeasy Mini Kit (Qiagen) according to the manufacturer's protocol. cDNA was synthesized starting from total RNA by QuantSeq 3' mRNA-Seq Library Prep Kits (Lexogen). After barcoding, the RNA libraries were pooled, denatured, and diluted to 2.4 pM final concentration. RNA-Seq was performed using NextSeq 550 (Illumina) set for 76 cycles in single end (SE), yielding an average of  $15 \times 10^6$  clusters for each sample. Sequences were aligned using STAR (version 2.5.3a) on the reference genome GRCm38; association between reads and genes was performed by featureCounts, using GENCODE (version M13) basic annotation as reference. Normalization and analysis of count data was performed using the R-package DESeq2 (version 1.0.19) (differential gene expression analysis based on the negative binomial distribution of counts data). The independent filtering of genes with low counts was set to a mean of 9 raw counts between all samples. The cutoff imposed for differential gene expression was the one suggested by the Sequencing Quality Control Consortium, which defines a gene as differentially expressed when it has an associated FDR value lower than 0.1 ( $P_{adj} < 0.1$ , Benjamini and Hochberg correction) and, at the same time, the absolute value of its log<sub>2</sub> fold change is greater

than 1 ( $\log_2 \text{FC} > 1$  or  $\log_2 \text{FC} < -1$ ). RNA-seq data are available at NCBI GEO (GEO accession number GSE183901).

### **Bioinformatics analysis**

Gene Set Enrichment Analysis (GSEAs) was conducted with the JAVA Web Start GSEA platform (v.4.0.3, <https://www.gsea-msigdb.org/gsea/index.jsp>) and using the GSEA pre-ranked module. Specifically, gene lists were obtained by performing differential gene expression (DGE) with DESeq2. Genes for which either FDR or  $\log_2\text{FC}$  statistics were not available due to outliers or low counts were discarded and the remaining genes were pre-ranked according to the  $\log_2\text{FC}$ . Statistics were calculated using gene set permutations ( $1 \times 10^3$ ) and the classic scoring scheme was utilized. To directly test whether transcriptional differences between *HW* and *HN* MBs correlated with molecular MB subgroups and subtypes, unbiased GSEA screens were performed against a total of 8 databases of gene sets (.gmx files), 4 of which directly derived from (5) (*i.e.* SHH, WNT, Group 3 and Group 4 subgroup signatures) and the remaining established by extracting SHH subtype-specific signatures (*i.e.* SHH $\alpha$ , SHH $\beta$ , SHH $\gamma$  and SHH $\delta$ ) from the dataset provided in (5) (GEO reference: GSE85217). The online tool GEO2R was used to perform DGE analysis between each SHH subtype versus the other 3 SHH subtypes. By R Studio (v.1.2.1335) and R (v.3.5.2), only genes with p-values  $< 0.001$  and upregulated in the considered subtype were selected for the signature.  $\log_2\text{FC}$  threshold was chosen to identify at least 20 genes for signature and ranged between 1 and 2. Each of the signature datasets was converted into murine orthologue genes by means of the online tool dbOrtho (<https://biodbnet-abcc.ncifcrf.gov/db/dbOrtho.php>). Genes that did not have corresponding murine orthologues were discarded. Gene sets with a nominal *P* value less than 0.05 and FDR-adjusted *q* value less than 0.25 were considered significant.

### **Quantitative PCR analysis**

Total RNA from mouse MBs was extracted using the RNeasy Mini kit (Qiagen, Chatsworth, CA, USA). One  $\mu\text{g}$  of total RNA was reverse-transcribed by using High-Capacity cDNA Reverse Transcription Kits (Applied Biosystems, Thermo Fisher Scientific). Quantitative real-time PCR was performed by using GoTaq® qPCR Master Mix (Promega), following manufacturer's instructions. Mouse-specific primers were purchased from Sigma-Aldrich.  $\beta$ -Actin was used as housekeeping gene.

### **Cell culturing**

Mouse cancer stem cells (CSCs) were generated at the Neural Stem Cell Biology Unit after dissociation of single tumors from *HW*, *HH* and *HN* mice and culturing under the conditions of the NeuroSphere Assay (25) (26). Human DAOY cells (kindly provided by Dr. Gaetano Finocchiaro, Fondazione IRCCS Istituto Neurologico "C. Besta", Milan, Italy) were grown as adherent monolayer in DMEM containing 20% FCS.

### **Evaluation of tumorigenicity**

For subcutaneous injection,  $3\text{-}5 \times 10^6$  mouse CSCs/human DAOY cells were transferred in 100-150  $\mu\text{l}$  of DMEM containing DNase (Sigma-Aldrich, St. Louis, MO) and injected into the right flank of 45-60 days old *nu/nu* and/or NSG mice. Mice were sacrificed at different time points comprised between 4-12 weeks post-injection, according to the cell line originally injected. For intracranial transplantation,  $2 \times 10^5$  CSCs were delivered into the right striatum by stereotactic injection through a 5  $\mu\text{l}$  Hamilton microsyringe. The following coordinates were used: AV= 0; ML= +2.5mm; DV= -3.5mm from bregma. Animals were sacrificed 2-6 months after transplantation.

### **Gene overexpression by viral transduction**

p53-null postnatal day 7 cerebellar neural stem cells (NSCs) and *HW*, *HH* and *HN* CSCs were infected with lentiviral vectors (LV) coding for *Rheb<sup>Q64L</sup>* (34) and/or retroviral vectors (RVs) coding for *Myc<sup>T58A</sup>* and DNp53-GFP (17) for 16 hours. GFP-coding LVs/RVs were used as mock controls.

### **Magnetic resonance imaging (MRI)**

All the MRI studies described in the paper were performed on a small animal-dedicated 7T scanner (30/70 BioSpec; Bruker, Ettlingen, Germany). The animal protocol used to monitor tumor development in *HW* and *HN* mice included high-resolution T2-weighted sequences (TR/TE = 3000/12 ms, matrix = 170×170, voxel size = 0.11 mm<sup>2</sup>, section thickness = 0.75 mm). After converting Bruker images into the nifti format with Matlab 2013 (MathWorks, Natick, Mass), tumor masses were manually segmented using ITK-SNAP (<http://www.itksnap.org>). Tumor volumes were then calculated by means of the '*fslstats*' tool of FSL (FMRIB software; Oxford Center for Functional MR Imaging of the Brain, Oxford, England).

### **Treatment of autochthonous, CSC- and DAOY-derived MBs with rapamycin**

For in vivo administration, rapamycin (LC Laboratories) was dissolved in 100% ethanol, stored at -20°C, and diluted in a vehicle solution containing 5% Tween-80 and 5% PEG 400 (Merck) immediately before injection. Autochthonous mice were randomized based on age and/or MRI analysis and then injected intraperitoneally with either 6 mg/kg of drug or vehicle for 5 days a week. Subcutaneous tumor-bearing mice were randomized when tumors, as measured by a caliper, reached 20 mm<sup>3</sup> in volume and then treated as described above.

### **Classification of human MB specimens**

Classification of human MB samples was performed by IHC using the WHO markers GAB1, Filamin A,  $\beta$ -catenin, p53 and c-Myc (51). Some samples from University of Brescia were also classified by nanoString technology.

### **Statistics**

Results for continuous variables were expressed as mean  $\pm$  standard error of the mean (SEM). Two-group comparisons were performed with the Student *t* test (independent samples, one tail or two tails, 95% confidence). In cases of not-normal distribution, the non-parametric Mann-Whitney test (non-equal SD and not normal distribution, two tails) was used.  $p < 0.05$  was considered statistically significant. \* $p < 0.05$ ; \*\* $p < 0.01$ ; \*\*\* $p < 0.005$ ; \*\*\*\* $p < 0.001$ .

### **Study approval**

All animal experiments were approved by and performed in accordance with the guidelines of the International Animal Care and Use Committee. The retrospective study on human MB samples was conducted in compliance with the Declaration of Helsinki and with policies approved by the Ethics Boards of Spedali Civili di Brescia, University of Brescia and Istituto Neurologico Besta, Milan, Italy. Specifically, for the retrospective and exclusively observational study on archival material obtained for diagnostic purposes, patient consent was not needed (Delibera del Garante n. 52 del 24/7/2008 and DL 193/2003).

### **Author contributions**

VC designed and performed experiments, acquired and analysed data, prepared the figures, and wrote the manuscript. MC, IP, FP, and VP performed experiments, acquired and analysed data.

ALG, GMS and ISP analysed molecular data. MZ, SM and MP performed experiments. BP, AF, AZ, AC, RM and PLP analysed histological, molecular, and imaging data. RG conceived and supervised the project, designed experiments, and wrote the manuscript.

### **Acknowledgements**

We thank Prof. Robert Wechsler-Reya for providing the retroviral constructs for *MycT58A* and *DNp53* to Alessio Zippo, and Tamara Canu for the expert assistance in the small animal 7 Tesla-based MRI acquisition carried out at the Preclinical Imaging Facility of the Experimental Imaging Center, established at the San Raffaele Scientific Institute and the Vita-Salute San Raffaele University. We also thank Gabriele Antonarelli for help with the production of the graphical abstract created with images from BioRender. The research leading to these results has received funding from Associazione Italiana Ricerca sul Cancro (AIRC) under IG 2015 - ID.16823 and IG 2019 - ID. 22904 projects, and by Associazione ‘*Dedicato A Te*’ to R.G.

### **Competing interests**

The authors have declared that no conflict of interest exists.

## References

1. Northcott PA, Robinson GW, Kratz CP, Mabbott DJ, Pomeroy SL, Clifford SC, et al. Medulloblastoma. *Nat Rev Dis Primers*. 2019;5(1):11.
2. Vladoiu MC, El-Hamamy I, Donovan LK, Farooq H, Holgado BL, Sundaravadanam Y, et al. Childhood cerebellar tumours mirror conserved fetal transcriptional programs. *Nature*. 2019.
3. Taylor MD, Northcott PA, Korshunov A, Remke M, Cho YJ, Clifford SC, et al. Molecular subgroups of medulloblastoma: the current consensus. *Acta Neuropathol*. 2012;123(4):465-72.
4. Schwalbe EC, Lindsey JC, Nakjang S, Crosier S, Smith AJ, Hicks D, et al. Novel molecular subgroups for clinical classification and outcome prediction in childhood medulloblastoma: a cohort study. *Lancet Oncol*. 2017;18(7):958-71.
5. Cavalli FMG, Remke M, Rampasek L, Peacock J, Shih DJH, Luu B, et al. Intertumoral Heterogeneity within Medulloblastoma Subgroups. *Cancer Cell*. 2017;31(6):737-54 e6.
6. Staedtke V, Dzaye O, and Holdhoff M. Actionable molecular biomarkers in primary brain tumors. *Trends Cancer*. 2016;2(7):338-49.
7. Louis DN, Perry A, Wesseling P, Brat DJ, Cree IA, Figarella-Branger D, et al. The 2021 WHO Classification of Tumors of the Central Nervous System: a summary. *Neuro Oncol*. 2021.
8. Kool M, Korshunov A, Remke M, Jones DT, Schlanstein M, Northcott PA, et al. Molecular subgroups of medulloblastoma: an international meta-analysis of transcriptome, genetic aberrations, and clinical data of WNT, SHH, Group 3, and Group 4 medulloblastomas. *Acta Neuropathol*. 2012;123(4):473-84.
9. Gajjar AJ, and Robinson GW. Medulloblastoma-translating discoveries from the bench to the bedside. *Nature reviews Clinical oncology*. 2014;11(12):714-22.
10. Zhukova N, Ramaswamy V, Remke M, Pfaff E, Shih DJ, Martin DC, et al. Subgroup-specific prognostic implications of TP53 mutation in medulloblastoma. *J Clin Oncol*. 2013;31(23):2927-35.
11. Garcia-Lopez J, Kumar R, Smith KS, and Northcott PA. Deconstructing Sonic Hedgehog Medulloblastoma: Molecular Subtypes, Drivers, and Beyond. *Trends Genet*. 2021;37(3):235-50.
12. Rudin CM, Hann CL, Laterra J, Yauch RL, Callahan CA, Fu L, et al. Treatment of medulloblastoma with hedgehog pathway inhibitor GDC-0449. *N Engl J Med*. 2009;361(12):1173-8.
13. Buonamici S, Williams J, Morrissey M, Wang A, Guo R, Vattay A, et al. Interfering with resistance to smoothed antagonists by inhibition of the PI3K pathway in medulloblastoma. *Sci Transl Med*. 2010;2(51):51ra70.
14. Kool M, Jones DT, Jager N, Northcott PA, Pugh TJ, Hovestadt V, et al. Genome sequencing of SHH medulloblastoma predicts genotype-related response to smoothed inhibition. *Cancer Cell*. 2014;25(3):393-405.
15. Skowron P, Farooq H, Cavalli FMG, Morrissy AS, Ly M, Hendrikse LD, et al. The transcriptional landscape of Shh medulloblastoma. *Nature communications*. 2021;12(1):1749.
16. Gibson P, Tong Y, Robinson G, Thompson MC, Currie DS, Eden C, et al. Subtypes of medulloblastoma have distinct developmental origins. *Nature*. 2010;468(7327):1095-9.

17. Pei Y, Moore CE, Wang J, Tewari AK, Eroshkin A, Cho YJ, et al. An animal model of MYC-driven medulloblastoma. *Cancer Cell*. 2012;21(2):155-67.
18. Kawauchi D, Robinson G, Uziel T, Gibson P, Rehg J, Gao C, et al. A mouse model of the most aggressive subgroup of human medulloblastoma. *Cancer Cell*. 2012;21(2):168-80.
19. Wetmore C, Eberhart DE, and Curran T. Loss of p53 but not ARF accelerates medulloblastoma in mice heterozygous for patched. *Cancer Res*. 2001;61(2):513-6.
20. Dimitrova V, and Arcaro A. Targeting the PI3K/AKT/mTOR signaling pathway in medulloblastoma. *Curr Mol Med*. 2015;15(1):82-93.
21. Wu CC, Hou S, Orr BA, Kuo BR, Youn YH, Ong T, et al. mTORC1-Mediated Inhibition of 4EBP1 Is Essential for Hedgehog Signaling-Driven Translation and Medulloblastoma. *Dev Cell*. 2017;43(6):673-88 e5.
22. Aldaregia J, Odriozola A, Matheu A, and Garcia I. Targeting mTOR as a Therapeutic Approach in Medulloblastoma. *Int J Mol Sci*. 2018;19(7).
23. Eckerdt F, Clymer J, Bell JB, Beauchamp EM, Blyth GT, Goldman S, et al. Pharmacological mTOR targeting enhances the antineoplastic effects of selective PI3K $\alpha$  inhibition in medulloblastoma. *Scientific reports*. 2019;9(1):12822.
24. Cancer M, Hutter S, Holmberg KO, Rosen G, Sundstrom A, Taylor J, et al. Humanized Stem Cell Models of Pediatric Medulloblastoma Reveal an Oct4/mTOR Axis that Promotes Malignancy. *Cell Stem Cell*. 2019;25(6):855-70 e11.
25. Ward RJ, Lee L, Graham K, Satkunendran T, Yoshikawa K, Ling E, et al. Multipotent CD15+ cancer stem cells in patched-1-deficient mouse medulloblastoma. *Cancer Res*. 2009;69(11):4682-90.
26. Corno D, Pala M, Cominelli M, Cipelletti B, Leto K, Croci L, et al. Gene Signatures Associated with Mouse Postnatal Hindbrain Neural Stem Cells and Medulloblastoma Cancer Stem Cells Identify Novel Molecular Mediators and Predict Human Medulloblastoma Molecular Classification. *Cancer Discov*. 2012;2(6):554-68.
27. Orr BA. Pathology, diagnostics, and classification of medulloblastoma. *Brain Pathol*. 2020;30(3):664-78.
28. Masuda T, Tsuda M, Yoshinaga R, Tozaki-Saitoh H, Ozato K, Tamura T, et al. IRF8 is a critical transcription factor for transforming microglia into a reactive phenotype. *Cell Rep*. 2012;1(4):334-40.
29. Feng Z, Hu W, de Stanchina E, Teresky AK, Jin S, Lowe S, et al. The regulation of AMPK beta1, TSC2, and PTEN expression by p53: stress, cell and tissue specificity, and the role of these gene products in modulating the IGF-1-AKT-mTOR pathways. *Cancer Res*. 2007;67(7):3043-53.
30. Kawamura T, Suzuki J, Wang YV, Menendez S, Morera LB, Raya A, et al. Linking the p53 tumour suppressor pathway to somatic cell reprogramming. *Nature*. 2009;460(7259):1140-4.
31. Tamayo-Orrego L, Wu CL, Bouchard N, Khedher A, Swikert SM, Remke M, et al. Evasion of Cell Senescence Leads to Medulloblastoma Progression. *Cell Rep*. 2016;14(12):2925-37.
32. Hemmesi K, Squadrito ML, Mestdagh P, Conti V, Cominelli M, Piras IS, et al. miR-135a Inhibits Cancer Stem Cell-Driven Medulloblastoma Development by Directly Repressing Arhgef6 Expression. *Stem Cells*. 2015.
33. Sutter R, Shakhova O, Bhagat H, Behesti H, Sutter C, Penkar S, et al. Cerebellar stem cells act as medulloblastoma-initiating cells in a mouse model and a neural stem cell signature characterizes a subset of human medulloblastomas. *Oncogene*. 2010;29(12):1845-56.

34. Magri L, Cambiaghi M, Cominelli M, Alfaro-Cervello C, Cursi M, Pala M, et al. Sustained activation of mTOR pathway in embryonic neural stem cells leads to development of tuberous sclerosis complex-associated lesions. *Cell Stem Cell*. 2011;9(5):447-62.
35. Kunkle A, De Preter K, Heukamp L, Thor T, Pajtler KW, Hartmann W, et al. Pharmacological activation of the p53 pathway by nutlin-3 exerts anti-tumoral effects in medulloblastomas. *Neuro Oncol*. 2012;14(7):859-69.
36. Jacobsen PF, Jenkyn DJ, and Papadimitriou JM. Establishment of a human medulloblastoma cell line and its heterotransplantation into nude mice. *J Neuropathol Exp Neurol*. 1985;44(5):472-85.
37. Hovestadt V, Ayrault O, Swartling FJ, Robinson GW, Pfister SM, and Northcott PA. Medulloblastomics revisited: biological and clinical insights from thousands of patients. *Nat Rev Cancer*. 2020;20(1):42-56.
38. Morrissy AS, Cavalli FMG, Remke M, Ramaswamy V, Shih DJH, Holgado BL, et al. Spatial heterogeneity in medulloblastoma. *Nat Genet*. 2017;49(5):780-8.
39. Neumann JE, Swartling FJ, and Schuller U. Medulloblastoma: experimental models and reality. *Acta Neuropathol*. 2017;134(5):679-89.
40. Liu GY, and Sabatini DM. mTOR at the nexus of nutrition, growth, ageing and disease. *Nat Rev Mol Cell Biol*. 2020.
41. Qin X, Jiang B, and Zhang Y. 4E-BP1, a multifactor regulated multifunctional protein. *Cell Cycle*. 2016;15(6):781-6.
42. Badodi S, Pomella N, Zhang X, Rosser G, Whittingham J, Niklison-Chirou MV, et al. Inositol treatment inhibits medulloblastoma through suppression of epigenetic-driven metabolic adaptation. *Nature communications*. 2021;12(1):2148.
43. Bhatia B, Northcott PA, Hambardzumyan D, Govindarajan B, Brat DJ, Arbiser JL, et al. Tuberous sclerosis complex suppression in cerebellar development and medulloblastoma: separate regulation of mammalian target of rapamycin activity and p27 Kip1 localization. *Cancer Res*. 2009;69(18):7224-34.
44. Agarwal S, Bell CM, Taylor SM, and Moran RG. p53 Deletion or Hotspot Mutations Enhance mTORC1 Activity by Altering Lysosomal Dynamics of TSC2 and Rheb. *Mol Cancer Res*. 2016;14(1):66-77.
45. Thompson EM, Ashley D, and Landi D. Current medulloblastoma subgroup specific clinical trials. *Transl Pediatr*. 2020;9(2):157-62.
46. Poschl J, Koch A, and Schuller U. Histological subtype of medulloblastoma frequently changes upon recurrence. *Acta Neuropathol*. 2015;129(3):459-61.
47. Hill RM, Kuijper S, Lindsey JC, Petrie K, Schwalbe EC, Barker K, et al. Combined MYC and P53 Defects Emerge at Medulloblastoma Relapse and Define Rapidly Progressive, Therapeutically Targetable Disease. *Cancer Cell*. 2015;27(1):72-84.
48. Kumar R, Smith KS, Deng M, Terhune C, Robinson GW, Orr BA, et al. Clinical Outcomes and Patient-Matched Molecular Composition of Relapsed Medulloblastoma. *J Clin Oncol*. 2021;JCO2001359.
49. Wu X, Northcott PA, Dubuc A, Dupuy AJ, Shih DJ, Witt H, et al. Clonal selection drives genetic divergence of metastatic medulloblastoma. *Nature*. 2012;482(7386):529-33.
50. Dickson D, Johnson J, Bergan R, Owens R, Subbiah V, and Kurzrock R. The Master Observational Trial: A New Class of Master Protocol to Advance Precision Medicine. *Cell*. 2020;180(1):9-14.

51. Ellison DW, Dalton J, Kocak M, Nicholson SL, Fraga C, Neale G, et al. Medulloblastoma: clinicopathological correlates of SHH, WNT, and non-SHH/WNT molecular subgroups. *Acta Neuropathol.* 2011;121(3):381-96.

Figure legends

Figure 1 - Autochthonous MBs developing in *Ptch1<sup>+/-</sup> p53<sup>-/-</sup>* mice show large cell/anaplastic histopathological features that are associated with mTORC1 hyperactivation

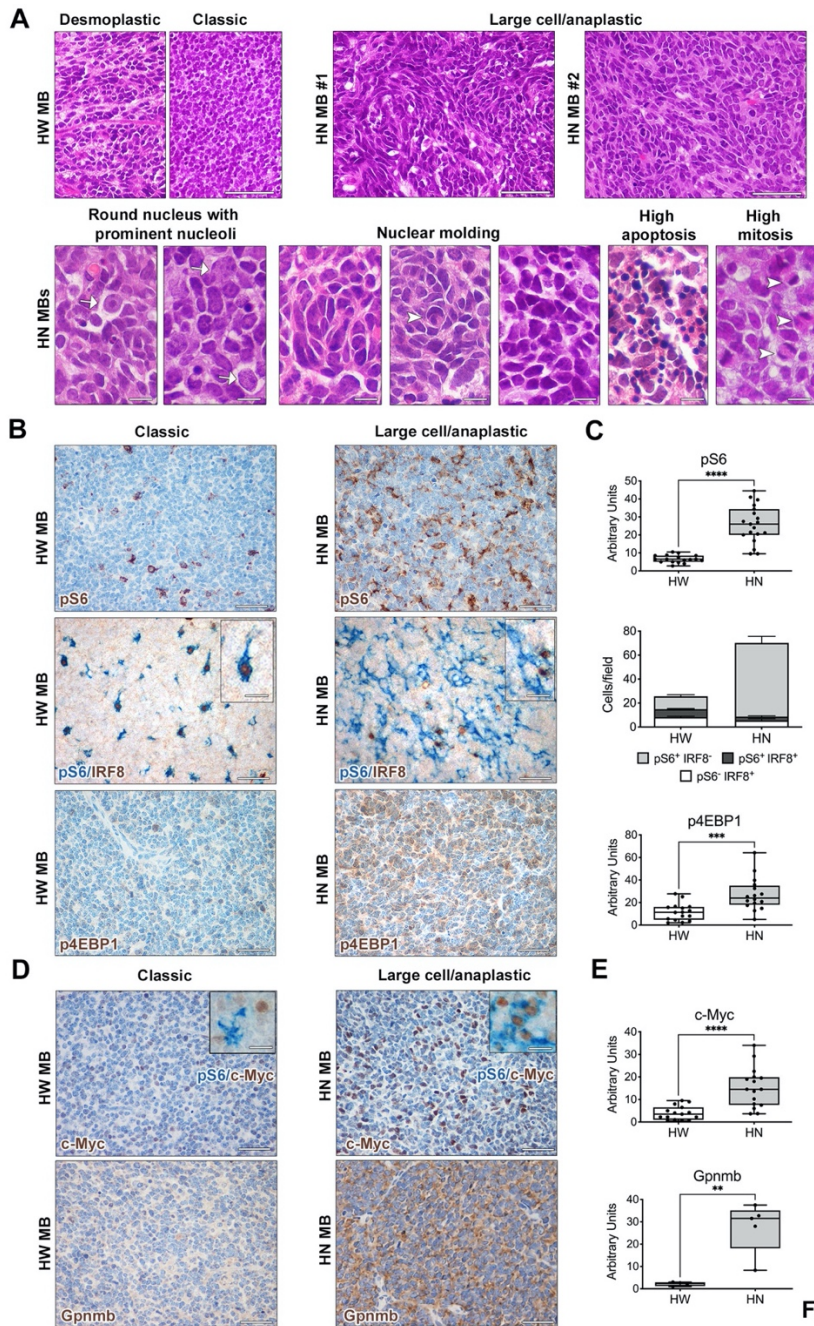


Fig. 1

(A) Typical features of desmoplastic MB (e.g. small undifferentiated cells interspersed in a dense neuropil) and of classic MB (e.g. small “blue” cells with round/ovoid nuclei) are found in *HW* MBs

(H&E). Conversely, histo-morphological *LC/A* characteristics are observed in *HN* MBs. Scale bars: 50  $\mu$ m. Traits typical of the large cell variant, as cells with round nuclei with prominent nuclei (white arrows), and of the anaplastic variant, as angular nuclei, nuclear wrapping (white arrowhead), nuclear molding, and frequent apoptotic and mitotic cells (white arrowheads), are detected in all *HN* MBs. Scale bars: 10  $\mu$ m.

**(B)** Higher numbers of cells hyperactivating pS6 (cytoplasmic staining, brown) are found in *HN LC/A* MBs than in *HW* MBs. The few pS6-IR cells (cytoplasmic staining, blue) in *HW* MBs are stromal cells, positive for the macrophage/microglia marker IRF8 (nuclear staining, brown). Conversely, most pS6-IR cells in *HN* MBs (cytoplasmic staining, blue) are tumor cells that do not express IRF8 (nuclear staining, brown). Increased activation of p4EBP1 is observed in *HN* MBs (cytoplasmic staining, brown). Scale bars: 50  $\mu$ m; insets: 10  $\mu$ m.

**(C)** Quantification of marker expression (shown as arbitrary units) and of cell subpopulations (shown as number of cells in a 60x microscopic field) is shown in the graphs.

pS6<sup>+</sup>IRF8<sup>-</sup> cells in *HW* vs. *HN* MBs: \*\*\*\*= $p < 0.0001$ , Student *t* test, unpaired.

**(D)** Increased c-Myc expression (nuclear staining, brown) is detected in *HN* MBs, with some c-Myc positive cells being also pS6-IR (cytoplasmic, blue; insets). mTORC1-regulated gene *Gpnmb* (cytoplasmic staining, brown) is upregulated in *HN* MBs. Scale bars: 50  $\mu$ m; insets: 10  $\mu$ m.

**(E)** Quantification of marker expression is shown in the graphs.

Quantitative data are represented as a box-and-whisker plot, with bounds from 25th to 75th percentile, median line, and whiskers ranging from minimum to maximum values. Student *t* test, unpaired.

**Figure 2 - The transcriptional signature of *HN* MBs is reminiscent of that of human SHH MBs with p53 mutation**

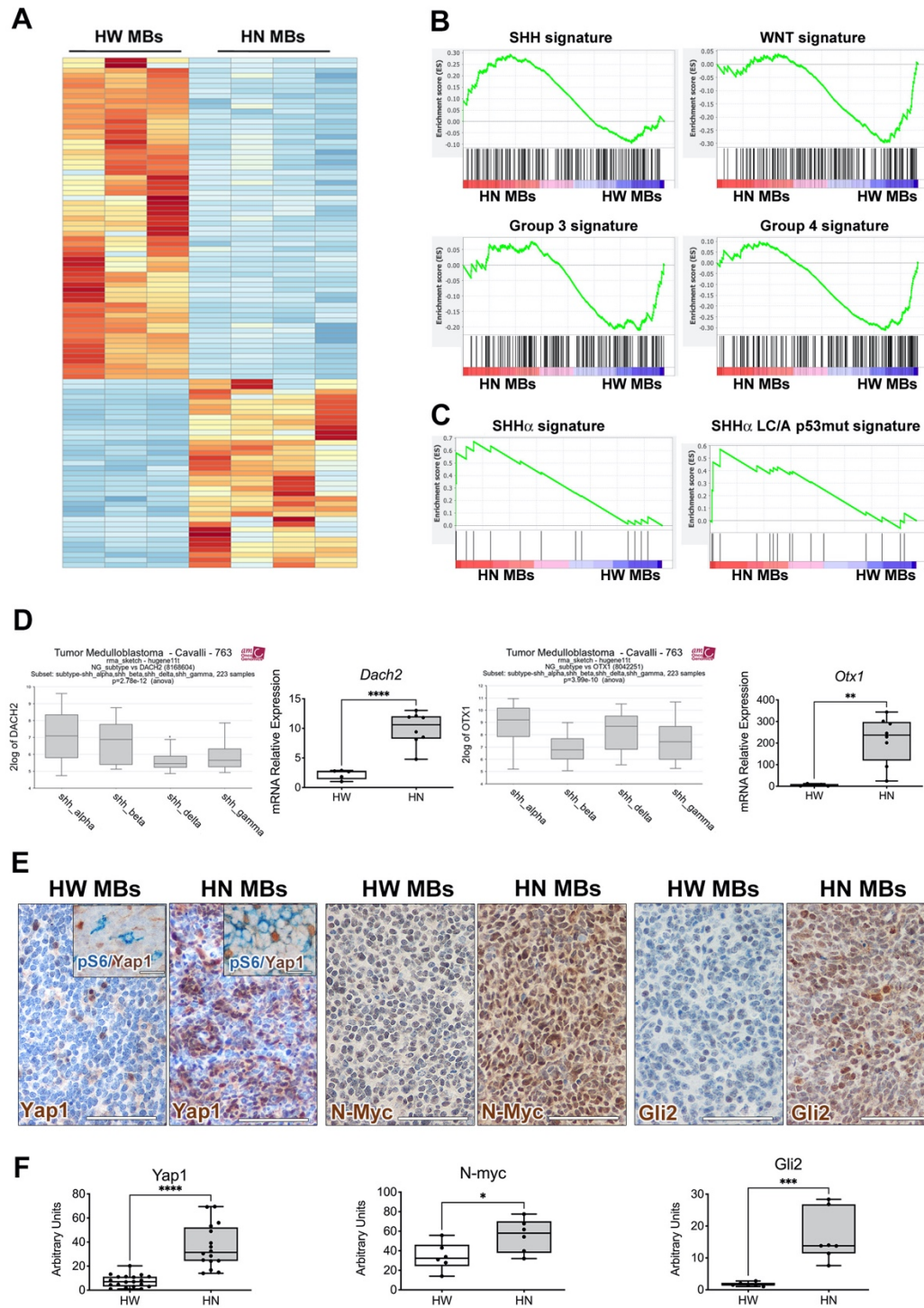


**Fig. 2**

**(A)** Supervised whole-transcript expression analysis of *HW* and *HN* MBs indicates that they are transcriptionally different.

**(B)** GSEA indicates that the gene set qualifying the human SHH subgroup is upregulated in *HN* MBs, whereas the gene sets qualifying the human WNT, Group 3 and Group 4 subgroups are upregulated in *HW* MBs.

**(C)** The gene sets qualifying the whole SHH $\alpha$  subtype and the SHH $\alpha$  subtype with p53 mutation and *LC/A* histology are significantly enriched in *HN* MBs.

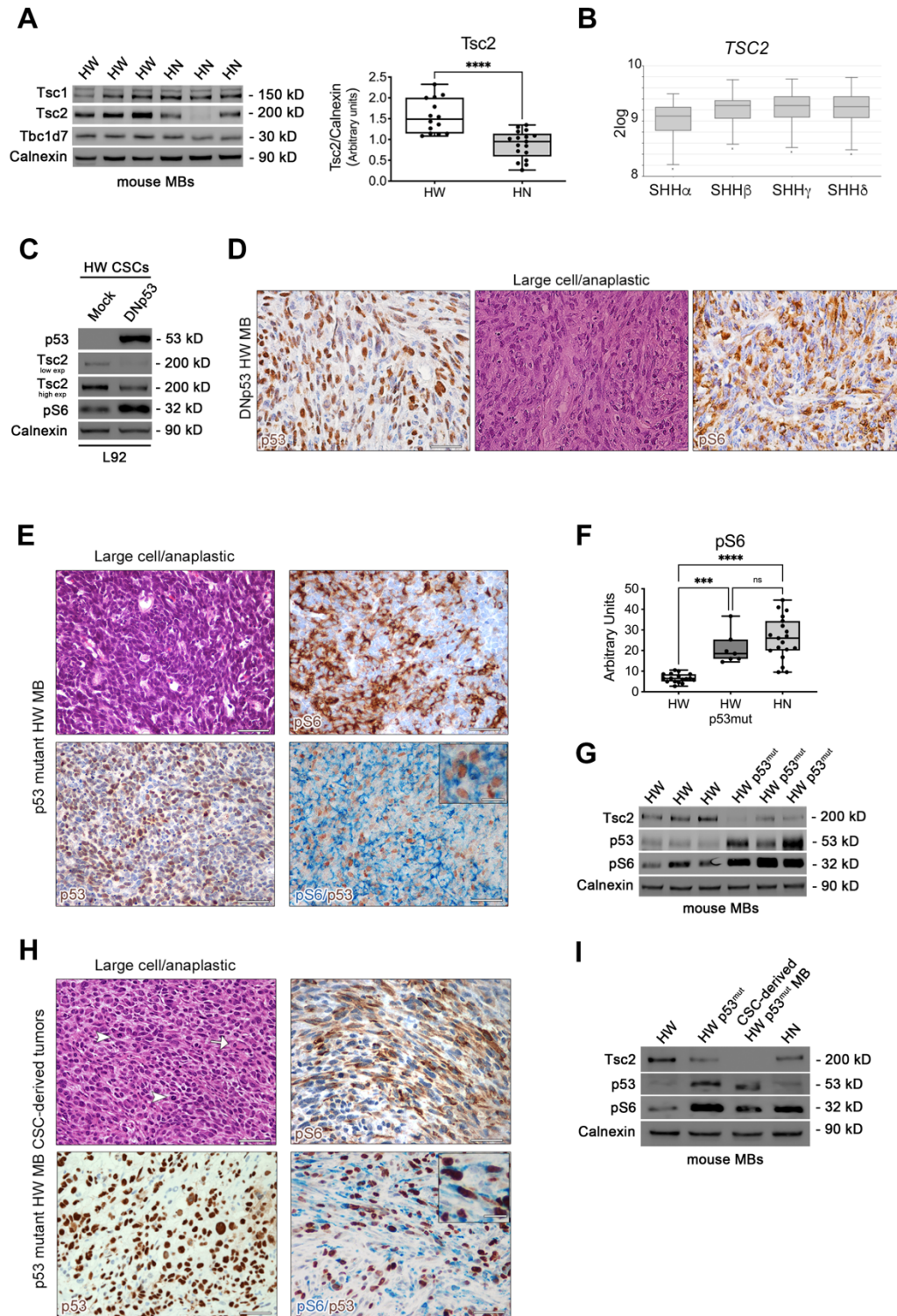
**(D)** *Dach2* and *Otx1* genes, which are significantly upregulated in the human SHH $\alpha$  subtype by *in silico* analysis of the dataset Tumor Medulloblastoma-Cavalli-763 by the R2 software (Genomics Analysis and Visualization Platform, <http://r2.amc.nl>; *DACH2*: SHH $\alpha$  vs. SHH $\delta$ :  $1.08e^{-09}$ ; SHH $\alpha$  vs. SHH $\gamma$ :  $1.27^{-07}$ ; *OTX1*: SHH $\alpha$  vs. SHH $\beta$ :  $2.22e^{-11}$ ; SHH $\alpha$  vs. SHH $\gamma$ :  $5.34e^{-06}$ ; Welch *t* test), are highly expressed in *HN* MBs (qPCR).

**(E)** The protein abundance of Yap1, N-Myc and Gli2 (nuclear staining, brown) is significantly enhanced in *HN* MBs, with some Yap1-positive cells being also immunoreactive for pS6 (cytoplasmic staining, blue). Scale bars: 50  $\mu$ m; insets: 10  $\mu$ m.

**(F)** Quantification of the level of marker expression is shown in the graphs.

Quantitative data are represented as a box-and-whisker plot, with bounds from 25th to 75th percentile, median line, and whiskers ranging from minimum to maximum values. Student *t* test, unpaired.

**Figure 3 - The expression of the negative mTORC1 regulator Tsc2 is significantly decreased in *HN* MBs and is regulated by p53**



- (A)** Protein level of the upstream mTORC1 regulators Tsc1, Tsc2 and Tbc1d7 in autochthonous MBs (WB). Densitometric quantification of Tsc2 in *HW* ( $n=14$ ) and *HN* MBs ( $n=17$ ).
- (B)** *TSC2* is expressed at significantly lower level in the human SHH $\alpha$  subtype than in the remaining subtypes (SHH $\alpha$  vs. SHH $\beta$ :  $1.44e^{-03}$ ; SHH $\alpha$  vs. SHH $\delta$ : T prob  $7.32e^{-05}$ ; SHH $\alpha$  vs. SHH $\gamma$ :  $3.3e^{-03}$ ; Welch *t* test).
- (C)** *HW* CSCs transduced with a dominant negative (DN) form of p53 show decreased levels of Tsc2 and enhanced pS6 activation.
- (D)** Tumors derived from DNp53 *HW* CSCs show high expression of the functionally inactive wildtype form of p53 (nuclear staining, brown), *LC/A* histology and mTORC1 hyperactivation, as indicated by many pS6-IR cells (cytoplasmic staining, blue). Scale bars: 50  $\mu$ m.
- (E)** Histological features of *LC/A* MBs are found in a subset of *HW* MBs characterized by spontaneously occurring p53 mutations (nuclear staining, brown). This phenotype correlates with the presence of pS6-IR cells, with many of them co-labelled with p53. Scale bars: 50  $\mu$ m; insets: 10  $\mu$ m.
- (F)** Quantification of pS6 staining is shown in the graphs and indicates that mTORC1 in p53 mutant *HW* MBs is hyperactivated as in *HN* MBs.
- (G)** Tsc2 levels in p53 mutant *HW* MBs are significantly lower than in *HW* MBs, while pS6 levels are increased.
- (H)** Anaplastic features and p53-IR cells are detected in tumors derived from a CSC line (L68) previously isolated from a p53 mutant *HW* MB. Many of the pS6-IR tumor cells observed are p53-IR. Scale bars: 50  $\mu$ m; insets: 10  $\mu$ m.
- (I)** Tsc2 levels in MBs derived from the CSC line L68 are significantly lower than in *HW* MBs, with pS6 activation being increased.

Quantitative data are represented as a box-and-whisker plot, with bounds from 25th to 75th percentile, median line, and whiskers ranging from minimum to maximum values. Student *t* test, unpaired (A). One-way ANOVA followed by Tukey's multiple comparison test (F).

Figure 4 - *HN* MB-derived CSCs give rise to *LC/A* MBs that hyperactivate mTORC1

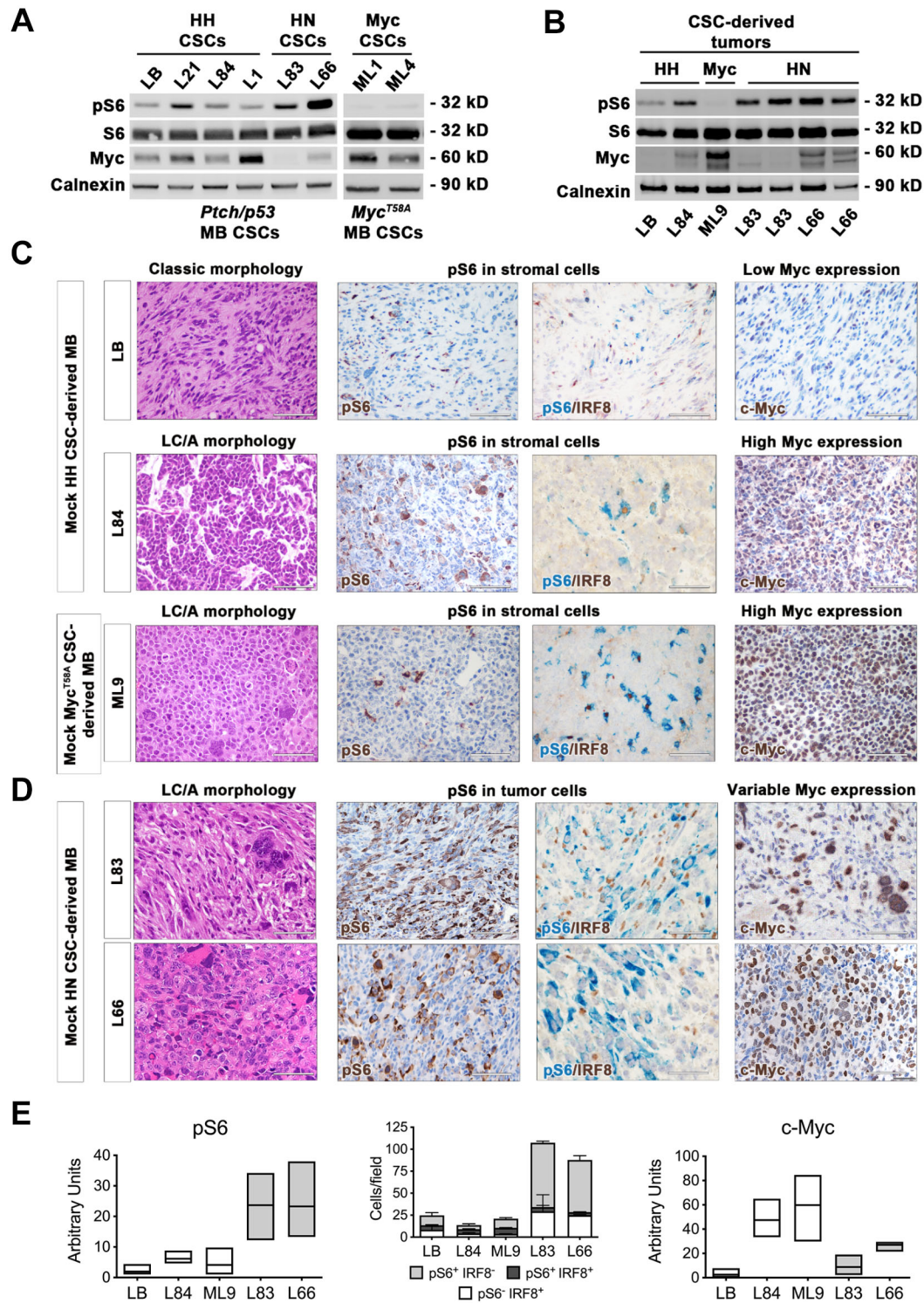


Fig. 4

**(A)** WB analysis shows significantly higher pS6 activation and lower Myc expression in *HN* CSC lines than in *HH* and Myc<sup>T58A</sup> CSC lines.

**(B)** WB analysis shows significantly higher pS6 activation and averagely lower Myc expression in tumors derived from the implantation of *HN* CSC lines than in those from *HH* and Myc<sup>T58A</sup> CSCs.

**(C)** H&E staining showing classic features in *HH* CSC-derived MBs, such as small cells intermingled with extensive neuropil (CSC line LB). Tumors from a subset of *HH* (CSC line L84) and from Myc<sup>T58A</sup> CSC lines (CSC line ML9) are endowed with *LC/A* characteristics, such as nuclear molding, prominent nucleoli, and apoptosis; in both cases, pS6-IR cells are few (cytoplasmic staining, brown) and are double-labelled with IRF8, indicating that they are tumor stromal cells (pS6, cytoplasmic staining, blue; IRF8, nuclear staining, brown). c-Myc (nuclear staining, brown) is lowly expressed in classic *HH* CSC-derived tumors, whereas it is very highly expressed in *LC/A* tumors derived from a subset of *HH* (CSC line L84) and from Myc<sup>T58A</sup> CSC lines (CSC line ML9). All scale bars: 50  $\mu$ m.

**(D)** Tumors from *HN* CSCs (CSC lines L83 and L66) show *LC/A* traits, as increased nuclear pleomorphism, presence of large cells and high level of cellular atypia. pS6 is hyperactivated in tumor cells (cytoplasmic staining, brown), as demonstrated by the absence of co-labelling of pS6-positive cells (cytoplasmic staining, blue) with IRF8 (nuclear staining, brown). c-Myc expression is found in medium-to-high number of cells. All scale bars: 50  $\mu$ m.

**(E)** Quantification of the level of marker expression is shown in the graphs.

Quantitative data are presented as floating bars from minimum to maximum values, line at mean. One-way ANOVA followed by Tukey's multiple comparison test. See Table S5 for detailed statistical analysis.

**Figure 5 - Enforced hyperactivation of mTORC1 in *HH/HN* CSCs increases tumor malignancy, induces an *LC/A* phenotype, and regulates MB subgroup specification by modulating the expression of subgroup-restricted markers**

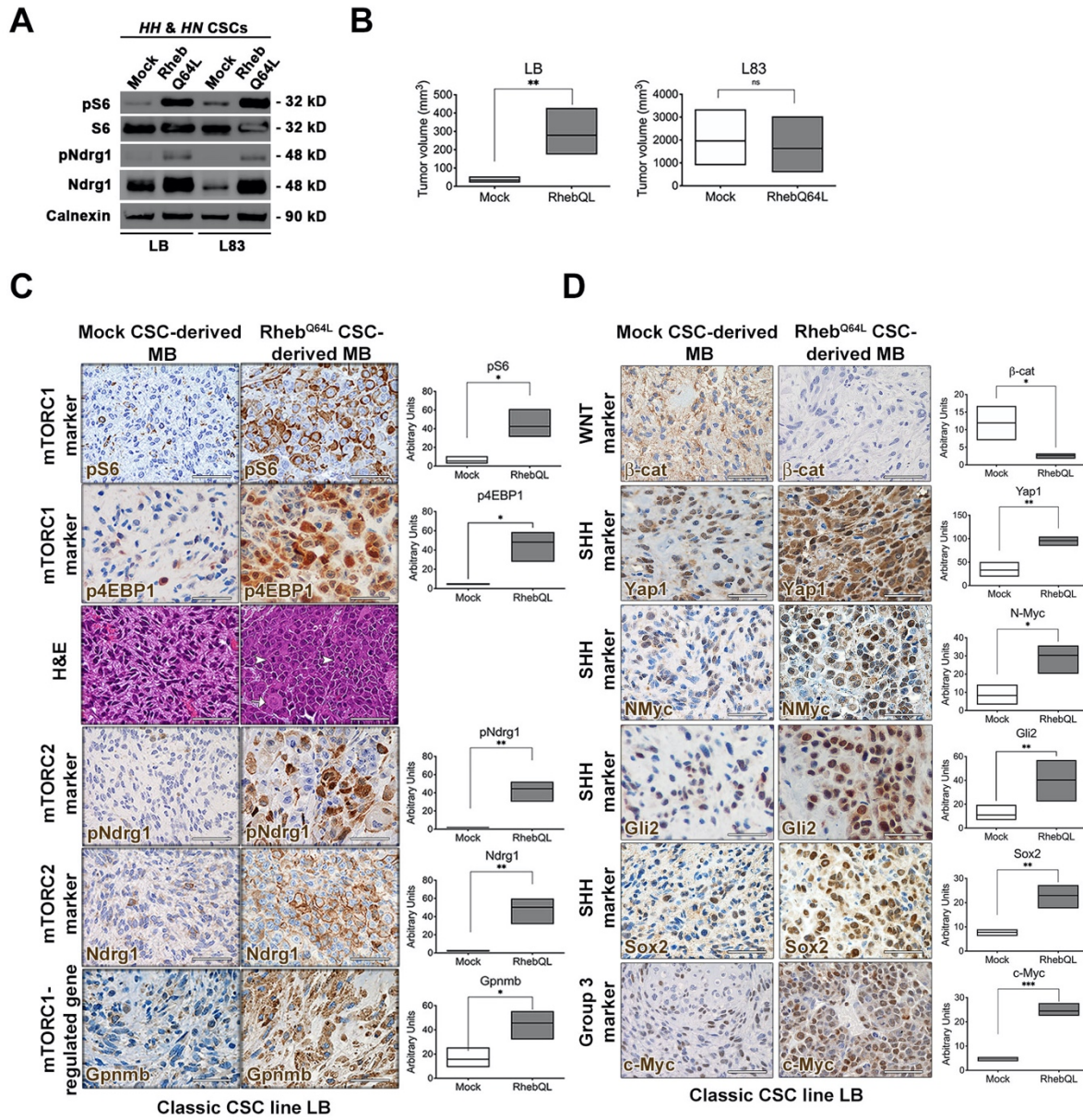


**Fig. 5**

**(A)** WB showing that mTORC1 hyperactivation in *HH/HN Rheb<sup>Q64L</sup>* CSC lines also promotes the activation of mTORC2 (*HH* CSC line LB and *HN* CSC line L83).

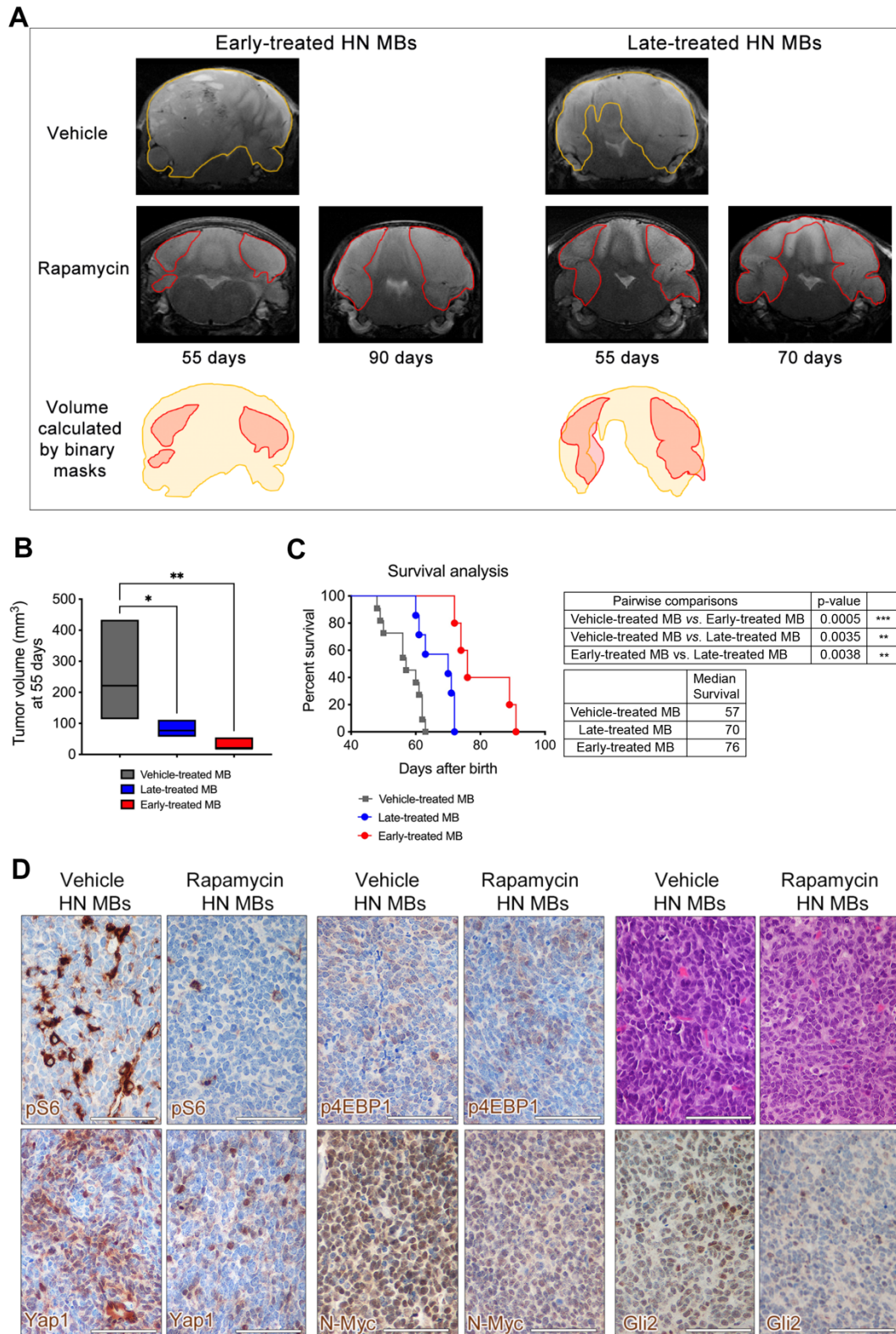
**(B)** Hyperactivation of *Rheb<sup>Q64L</sup>* in *classic HH* CSCs (LB) give rise to tumors that grow faster and larger than controls (volume measured at 54 days post-transplant for LB). The same hyperactivation in *LC/A HN* CSCs (L83) does not significantly affect the rate of tumorigenesis (volume measured at 83 days post-transplant for L83).

**(C)** H&E staining showing pS6 and p4EBP1 hyperactivation in tumor cells in MBs derived from *classic HH* CSCs (LB) after transduction with *Rheb<sup>Q64L</sup>*. *HH Rheb<sup>Q64L</sup>* MBs are endowed with typical *LC/A* features, *e.g.* nuclear molding, large cells (white arrow), several mitotic figures (white arrowheads), *etc.* The mTORC2 marker pNdrG1 is also strongly hyperactivated in *HH Rheb<sup>Q64L</sup>* MBs. The mTORC1 regulated gene *Gpnmb* is highly expressed in *Rheb<sup>Q64L</sup>* MBs. All scale bars: 50  $\mu$ m. Quantification of the level of marker expression (shown as arbitrary units) is shown in the graphs (right panels).

**(D)** The WNT-associated classifier  $\beta$ -catenin is significantly downregulated in *Rheb<sup>Q64L</sup> HH* CSC-derived MBs (CSC line LB), whereas markers typical of p53 mutant SHH MBs, such as *Yap1*, *N-Myc*, *Gli2* and *Sox2*, are upregulated. The Group 3 classifier *c-Myc* is also overexpressed in *Rheb<sup>Q64L</sup> HH* CSC-derived MBs. All scale bars: 50  $\mu$ m. Quantification of the level of marker expression (shown as arbitrary units) is shown in the graphs (right panels).

Quantitative data are presented as floating bars from minimum to maximum values, line at mean. Student *t* test, unpaired. See Table S5 for detailed statistical analysis.

**Figure 6 - Pharmacological targeting of the mTOR pathway hampers the growth of autochthonous SHH-TP53 mutant MBs**



**(A)** Longitudinal T2-weighted MRI analysis indicates that rapamycin administration significantly impairs the growth of early- and late-stage *HN* MBs.

**(B)** MB volume, as calculated by binary masks at day 55 of age, *i.e.* the MRI time point closer to the median survival of control mice, is significantly reduced by both rapamycin treatment regimens when compared to vehicle-treated controls (late-treated *HN* MBs, \*:  $p < 0.05$ ; early-treated *HN* MBs, \*\*:  $p < 0.01$ ). At the latest time points assessed for early (90 days) and late-treated (70 days) *HN* MBs, both treated *HN* MBs are significantly smaller than controls at 55 days. Statistical analysis is shown in the upper right table.

**(C)** Kaplan-Meier survival curves show that the lifespan of *HN* mice treated with rapamycin at early and late stages of tumor development is significantly increased as compared to control mice ( $n=11$  per vehicle-treated mice,  $n=5$  for early-treated mice,  $n=7$  for late-treated mice).

**(D)** Following late rapamycin treatment, *HN* MBs show a significant reduction in the activation of pS6, but not of p4EBP1, in nuclear pleomorphism and molding, and in Yap1, N-Myc and Gli2 expression. All scale bars: 50  $\mu\text{m}$ .

Quantitative data are presented as floating bars from minimum to maximum values, line at mean.

One-way ANOVA followed by Dunnett's multiple comparison test (B). Log rank test (C).

**Figure 7 - Pharmacological targeting of the mTOR pathway significantly impairs the growth of CSC-derived mTOR-driven LC/A MBs but not that of MBs belonging to other subgroups**

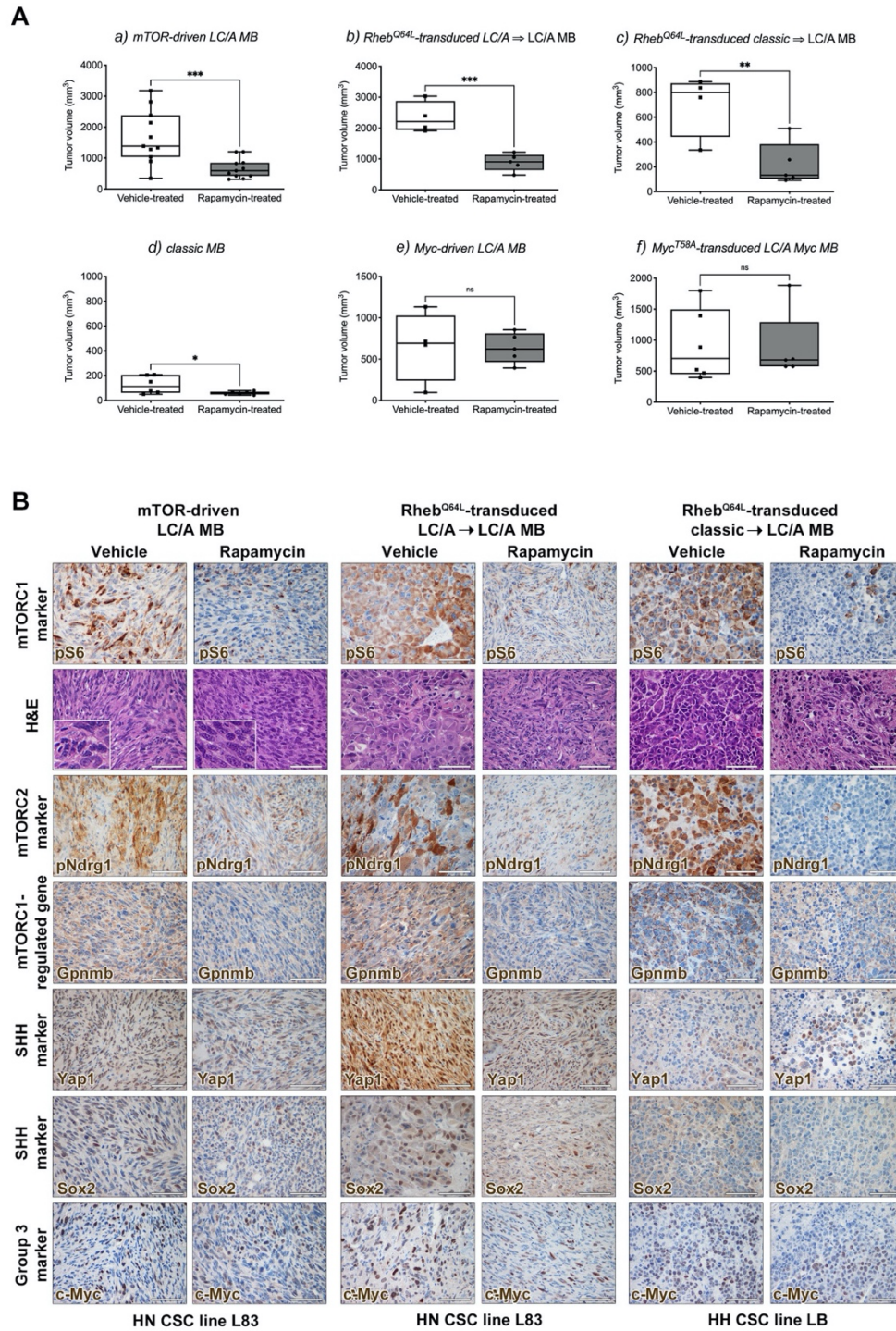


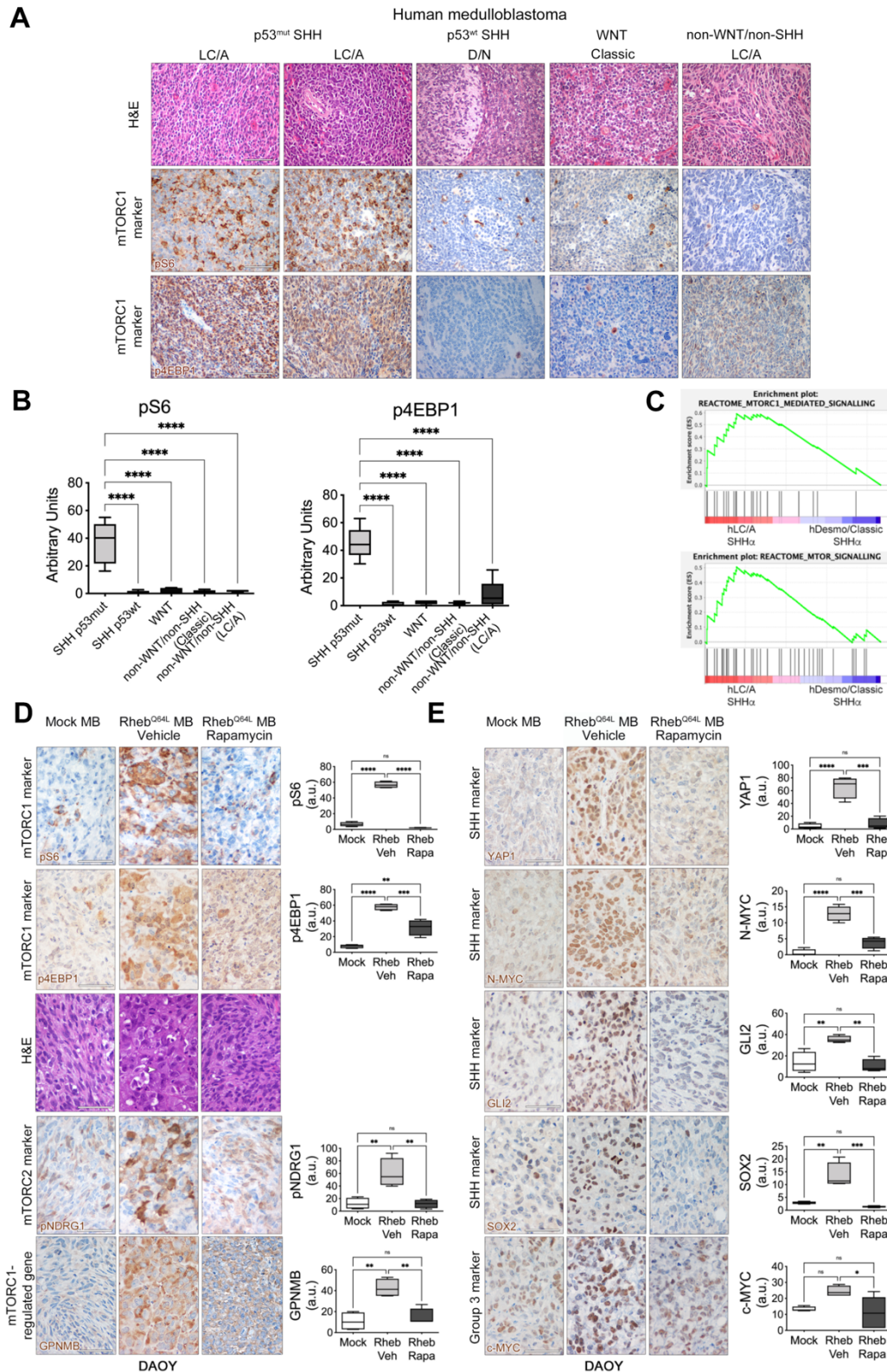
**Fig. 7**

**(A)** Tumor growth is significantly reduced by rapamycin treatment in *LC/A* tumors generated by *a)* *HN* CSCs with endogenous activation of mTORC1 (L83 and L66, 28 days of treatment for both vehicle and rapamycin arms;  $n=11$ ), *b)* the same CSCs transduced with *Rheb*<sup>Q64L</sup> (L83, 25 days of treatment for both vehicle and rapamycin arms;  $n=5$ ), and *c)* *classic HH* CSCs transduced with *Rheb*<sup>Q64L</sup> (17 days of treatment for vehicle arm; 30 days of treatment for rapamycin arm;  $n=6$ ). Conversely, tumor growth was only slightly affected by rapamycin treatment in *d)* *classic* tumors generated by *classic HH* CSCs (LB, 30 days of treatment for both vehicle and rapamycin arms;  $n=6$ ). No significant differences in tumor volume were detected in *LC/A* tumors induced by *e)* *HH* CSCs with no endogenous hyperactivation of mTORC1 (L84, 40 days of treatment for both vehicle and rapamycin arms;  $n=5$ ) and *f)* *Myc*<sup>T58A</sup>-transduced CSCs (ML9, 20 days of treatment for both vehicle and rapamycin arms;  $n=6$ ).

**(B)** H&E analysis following rapamycin treatment of the different types of *LC/A* MBs shows a significant reduction in nuclear pleomorphism (insets in mTOR-driven *LC/A* MB, left panels), in nuclear molding and in cell size (middle and right panels). Activation of both pS6 and pNdrp1 was strongly decreased by treatment, and so it was the expression of Gpnmb, Yap1 and Sox2. All scale bars: 50  $\mu\text{m}$ .

Quantitative data are represented as a box-and-whisker plot, with bounds from 25th to 75th percentile, median line, and whiskers ranging from minimum to maximum values. Student *t* test, unpaired.

**Figure 8 - mTORC1 activation is specifically found in human p53 mutant SHH MBs with LC/A component and may be a subgroup-specific therapeutic vulnerability**



**(A)** High numbers of tumor cells positive for the mTORC1 surrogate markers pS6 and p4EBP1 (cytoplasmic staining, brown) are observed only in human *LC/A* MBs belonging to the SHH subgroup with p53 mutation and are not detected in human desmoplastic/nodular (D/N) SHH p53wt, classic WNT, and *LC/A* non-WNT/non-SHH MBs. Scale bars: 50  $\mu$ m.

**(B)** Quantification of pS6 and p4EBP1 expression in the different subgroups. Only statistically significant pairwise comparisons are shown.

**(C)** Tumors from human DAOY cells after *Rheb<sup>Q64L</sup>* transduction show increased frequency of pS6- and p4EBP1-IR tumor cells, which are very few in mock tumors and are reduced in number after treatment with rapamycin. *Rheb<sup>Q64L</sup>* transduction promotes the acquisition of *LC/A* traits, such as the presence of large cells with prominent nucleoli (white arrowheads), which are not observed in controls and are strongly diminished by rapamycin (H&E). The activation of pNDRG1 and the expression of GPNMB are both increased in *Rheb<sup>Q64L</sup>*-transduced MBs and turned off by rapamycin. Scale bars: 50  $\mu$ m. Quantification of the level of marker expression is shown in the graphs.

**(D)** The expression of YAP1, N-MYC, GLI2, SOX2 and c-MYC is enhanced by mTORC1 hyperactivation and decreased by rapamycin administration. Scale bars: 50  $\mu$ m. Quantification of the level of marker expression is shown in the graphs.

Quantitative data are represented as a box-and-whisker plot, with bounds from 25th to 75th percentile, median line, and whiskers ranging from minimum to maximum values. One-way ANOVA followed by Tukey's multiple comparison test.